Light Manipulation and Applications

Science Exploration

Open Access Review

# Nonlinear optical field engineering with lithium niobate metasurfaces

Hongyu Sun[1], Haigang Liu[2,*], Xianfeng Chen[1,2,3,*]

[1]Shandong Provincial Key Laboratory of Light Field Manipulation Physics and Applications & School of Physics and Optoelectronics, Shandong Normal University, Jinan 250358, Shandong, China.
[2]State Key Laboratory of Advanced Optical Communication Systems and Networks, School of Physics and Astronomy, Shanghai Jiao Tong University, Shanghai 200240, China.
[3]Shanghai Research Center for Quantum Sciences, Shanghai 201315, China.

***Correspondence to:** Haigang Liu, State Key Laboratory of Advanced Optical Communication Systems and Networks, School of Physics and Astronomy, Shanghai Jiao Tong University, Shanghai 200240, China. E-mail: liuhaigang@sjtu.edu.cn
Xianfeng Chen, Shandong Provincial Key Laboratory of Light Field Manipulation Physics and Applications & School of Physics and Optoelectronics, Shandong Normal University, Jinan 250358, Shandong, China; State Key Laboratory of Advanced Optical Communication Systems and Networks, School of Physics and Astronomy, Shanghai Jiao Tong University, Shanghai 200240, China; Shanghai Research Center for Quantum Sciences, Shanghai 201315, China. E-mail: xfchen@sjtu.edu.cn

**Received:** February 05, 2026 **Accepted:** May 28, 2026 **Published:** June 05, 2026

**Cite this article:** Sun H, Liu H, Chen X. Nonlinear optical field engineering with lithium niobate metasurfaces. Light Manip Appl. 2026;1:202603. https://doi.org/10.70401/lma.2026.0013

## Abstract

Metasurfaces composed of subwavelength-scale artificial meta-atoms have emerged as a powerful platform for manipulating light. By enabling strong light-matter interactions within ultrathin planar geometries, metasurfaces have opened new avenues for highly integrated photonic devices. Lithium niobate ($LiNbO_3$) is considered one of the most promising multifunctional integrated photonic platforms due to its outstanding properties, such as a large second-order nonlinear susceptibility, a broad transparency window, and a strong electro-optic (EO) effect. In recent years, integrated photonic devices based on lithium-niobate-on-insulator platforms have experienced rapid development. This review summarizes recent advances in $LiNbO_3$ metasurfaces, providing a comprehensive overview of their demonstrated applications in nonlinear frequency conversion, wavefront and phase modulation, and dynamic EO modulation. By systematically introducing the interplay between the intrinsic material properties of $LiNbO_3$ and the structural design principles of metasurfaces, this review offers a coherent framework for understanding their nonlinear and active optical functionalities, and serves as a valuable reference for the design and implementation of nonlinear and actively tunable micro- and nano-photonic devices.

**Keywords:** Lithium niobate, metasurfaces, nonlinear optics, electro-optic effect, phase manipulation

## 1. Introduction

Conventional optical components manipulate light through propagation in bulk media, often leading to bulky footprints unsuitable for modern integrated photonic systems[1,2]. Over the past decade, optical metasurfaces have ushered in a paradigm shift by enabling flexible control over electromagnetic fields at subwavelength scales[1,3-11]. Metasurfaces are two-dimensional structures composed of subwavelength units, which enable precise, subwavelength-scale control over the polarization, phase, and amplitude of electromagnetic waves through the rational design of their geometric parameters[12-18].

This class of micro- and nano-structured artificial media has attracted great interest during the past 15 years and yielded ground-breaking electromagnetic and photonic phenomena[3,4,19-25]. This is very appealing for photonic applications that require a high degree of integration, such as ultracompact laser cavities (e.g., vertical cavity surface-emitting lasers)[26]. Meanwhile, given their two-dimensional character, metasurfaces can be easily made multifunctional by stacking multiple elements in series, offering new degrees of freedom for integrated photonics[1,10,25,27-37].

Metasurfaces also hold significant importance in the field of nonlinear optics (NLO), as they can mitigate or even completely overcome phase-matching requirements to a certain extent, thereby exhibiting strong NLO responses[29,32]. This departure from the stringent phase-matching requirements of bulk crystals is attributed to two fundamental mechanisms at the subwavelength scale. First, the physical thickness (L) of a metasurface is typically in the nanometer regime, which is orders of magnitude smaller than the

coherence length that generally falls on the micrometer scale ($L_c = \pi/\Delta k$), where $\Delta k = k_{2\omega} - 2k_{\omega}$ represents the intrinsic phase mismatch between the fundamental and harmonic waves. This means that the phase mismatch does not have sufficient distance to accumulate and cause destructive interference. Second, the periodic arrangement of meta-atoms provides reciprocal lattice vectors (G) that can compensate for this momentum mismatch ($\Delta k = k_{2\omega} - 2k_{\omega} - G = 0$), enabling momentum-driven phase matching within a subwavelength interaction volume. But at the same time, it also raises another important issue. The dramatic reduction in light-matter interactions caused by the intrinsic down-sizing of the interaction volume decreases the efficiency of nonlinear processes. Therefore, to overcome this bottleneck and obtain efficient NLO processes in meta-optics, alternative approaches must be devised to enhance the light-matter interaction over subwavelength distances[38-44]. Plasmonic metasurfaces were initially proposed to tackle the challenges of subwavelength light-matter interactions by leveraging the collective oscillations of electron-photon modes in metallic nanostructures[15,45,46]. These materials enable extreme local field confinement, facilitating significant breakthroughs in nonlinear amplification[47-49], high-sensitivity sensing[50-52], and quantum optics[53,54]. However, the performance of plasmonic devices is intrinsically limited by significant ohmic losses at optical frequencies, resulting in low quality (Q) factors that hinder their use in high-efficiency functional nanophotonics. Furthermore, the high cost of precious metals such as Au and Ag, together with their incompatibility with complementary metal-oxide-semiconductor processes, remains a major barrier to scalable manufacturing. Consequently, dielectric metasurfaces compatible with semiconductor processes have emerged as a research hotspot[55,56]. Dielectric metasurfaces are typically composed of dielectric or semiconductor materials with high refractive indices and high nonlinear coefficients (such as Si, GaAs, $TiO_2$, etc.). These materials typically exhibit low optical loss at optical frequencies and possess high refractive index contrast with the surrounding medium. This enables excitation of magnetic field resonance modes alongside electric field resonance modes, allowing electromagnetic resonance to manipulate optical properties and achieve localized electromagnetic field enhancement. Consequently, dielectric metasurfaces demonstrate exceptional optical performance across numerous fields[39,57-61].

To date, semiconducting metasurfaces have been successfully applied to nonlinear frequency conversion and light-by-light modulation. However, in applications within the field of nonlinear optics, constraints imposed by the intrinsic properties of materials remain a challenge. III-V semiconductor materials with non-centrosymmetric crystal structures (such as GaAs) possess high nonlinear coefficients, but their narrow bandgap renders them unsuitable for applications in the visible spectrum. Therefore, the search for dielectric materials with more comprehensive functionality is particularly crucial. Among the various materials under explored, lithium niobate ($LiNbO_3$, LN) is widely regarded as an ideal candidate for such applications. $LiNbO_3$ is a multifunctional crystal with many outstanding optical properties[62]. It is transparent across a broad spectral range from ultraviolet (UV) to mid-infrared, and possesses a large $X^{(2)}$ nonlinear tensor. Moreover, $LiNbO_3$ exhibits outstanding electro-optic (EO) properties along with exceptional acousto-optic and piezoelectric characteristics[63], earning it the title of "optical silicon"[64]. These properties make $LiNbO_3$ an attractive material for photonics applications in general and for nano-optics in particular. However, a significant challenge for uses in nano-optics is posed by the relatively low refractive index, which spans from 2.2 in the near-infrared to 2.4 in the visible spectral range. This moderate index contrast limits the ability to tightly confine light within subwavelength volumes, resulting in weaker geometrical resonances (such as Mie resonances) compared to high-index materials like silicon. Yet, the aforementioned properties largely outweigh this drawback in a broad set of applications. In Table 1, we compare the optical properties of $LiNbO_3$ with other materials (such as GaAs, GaP, AlN, and Si) commonly used for nonlinear optics and electro-optics at the nanoscale. While semiconducting materials have higher refractive indices and second-order nonlinearities, most of them have limited application in the visible-UV spectral range, due to their typically high absorption. Furthermore, the often-used III-V semiconductors feature a crystalline structure that provides nonlinear coupling only between three different components of the electric field. This feature makes it challenging to take full advantage of their large nonlinearity with co-polarized beams. Finally, $LiNbO_3$ provides unique means for fast dynamic modulation of the material properties by the EO effect, which enables tuning the refractive index by an externally applied voltage with frequencies well-above gigahertz (GHz). Despite its promising prospects, nanofabrication of $LiNbO_3$ poses significant challenges compared to silicon or silicon nitride due to its chemically inert and highly hard nature. In recent years, with the maturation of lithium niobate on insulator technology and breakthroughs in micro/nanofabrication processes such as ion beam etching and chemical mechanical polishing, the application of $LiNbO_3$ to meta-optics has been theoretically[64-66] and experimentally[40,67-72] investigated. These preliminary studies have already highlighted the potential of $LiNbO_3$ metasurfaces for nonlinear and tunable meta-optics in the NIR and visible range.

**Table 1.** Linear and nonlinear optical properties of $LiNbO_3$ compared to other widely used dielectric materials.

| Material | Refractive index at $\lambda$ = 1,550 nm | Transparency window (um) | Absorption coefficient at the 1,550 nm ($cm^{-1}$) | Largest nonlinear susceptibility (pm/V or $m^2/V^2$) | EO coefficient (pm/V) |
|---|---|---|---|---|---|
| $LiNbO_3$ | ~2.2 | 0.35-4.5 | < 0.001 | $d_{33} \approx 21$ | $r_{33} \approx 31$ |
| Si | ~3.5 | 1-8 | < 0.001 | $X^{(3)} \approx 2.8 \times 10^{-18}$ | - |
| GaAs | ~3.5 | 0.9-18 | < 0.001 | $d_{36} \approx 170$ | $r_{41} \approx 1.5$ |

| | | | | | |
|---|---|---|---|---|---|
| $TiO_2$ | ~2.4 | 0.4-5 | < 0.001 | $X^{(3)} \approx 10^{-19}$-$10^{-18}$ | - |
| GaP | ~3.1 | 0.45-14 | < 0.001 | $d_{36} \approx 70$ | $r_{41} \approx -1$ |
| GaN | ~2.3 | 0.37-7 | < 0.001 | $d_{33} \approx 10$ | $r_{33} \approx 1.9$ |

EO: electro-optic; Si: silicon; GaAs: gallium arsenide; $TiO_2$: titanium dioxide; GaP: gallium phosphide; GaN: gallium nitride.

Here, we provide a systematic review of recent advancements in $LiNbO_3$ metasurfaces, spanning both fabrication methodologies and device functionalities. The remainder of this review is organized as follows. Section 2 describes the fabrication techniques for $LiNbO_3$ metasurfaces, covering both top-down and bottom-up approaches, thereby laying the material and structural foundation for subsequent discussions. Section 3 examines the enhancement of second-order up-conversion processes, specifically second harmonic generation (SHG) and sum-frequency generation (SFG), enabled by these platforms, with an emphasis on two categories of resonance mechanisms: localized resonances (e.g., Mie-type, toroidal dipole, and anapole resonances) and nonlocal resonances (e.g., bound states in the continuum (BICs) and guided-mode resonances (GMRs)), followed by a comparative analysis of their efficiencies and fabrication trade-offs. Building on this nonlinear foundation, Section 4 explores emerging parametric down-conversion and higher-order multiphoton processes, including difference-frequency generation (DFG), spontaneous parametric down-conversion (SPDC), and high-harmonic generation (HHG). Section 5 addresses static phase modulation mechanisms, discussing how resonant phase and the Pancharatnam-Berry (PB) phase can be harnessed to achieve precise wavefront control and construct advanced nonlinear metalenses. Section 6 then focuses on dynamically adjustable $LiNbO_3$ metasurfaces, highlighting high-speed EO tuning strategies for the active modulation of optical phase, intensity, and resonance conditions. Finally, Section 7 summarizes the practical challenges facing current $LiNbO_3$ metasurface research, such as thermal stability, fabrication yield, and scalable photonic integration, and provides an outlook on promising future research trajectories.

## 2. Preparation Methods

Conventional $LiNbO_3$ devices are primarily fabricated from bulk crystals, typically characterized by millimeter-scale dimensions that are incompatible with the rigorous demands of modern integration and miniaturization. In recent years, the rapid advancement of thin-film lithium niobate (TFLN) technology has established new paradigms for the development of high-density integrated $LiNbO_3$ devices[73,74]. Sub-micron-scale, high-Q single-crystal $LiNbO_3$ films have been successfully realized through advanced fabrication techniques, including crystal ion slicing, molecular beam epitaxy, and chemical vapor deposition[75,76]. These approaches not only preserve the intrinsic superior properties of $LiNbO_3$ but also facilitate a significant reduction in device footprint, thereby promoting the advancement of large-scale integrated photonic circuits. In this part, we classify fabrication methods into two major categories: top-down, whereby parts of the material of interest are deterministically removed; and bottom-up, whereby chemicals assemble into micro- and/or nanostructures.

### 2.1 Top-down

One of the mainstream methods for fabricating deterministic structures is focused ion beam (FIB) etching. FIB milling uses ions (typically $Ga^+$) accelerated to energies of around 30 keV to bombard the surface of a material and sputter it, as sketched in Figure 1A. This approach is relatively straightforward, does not require a mask, offers a high resolution (10-15 nm) and produces structures with steep side-walls ($\approx 84°$)[68,77]. However, FIB is based on point-wise ablation, which is time-consuming and costly, thus making it not suitable for patterning large areas approaching the $mm^2$ scale. Other limitations of FIB are the surface roughness, which can spoil the resonators' performances, and the $Ga^+$ contamination, which introduces defects within the crystal lattice. These problems can be lessened to some extent by optimizing the FIB operating parameters and by introducing a sacrificial/protective layer that has also the function of preventing charge accumulation and can be removed in a post processing step[68].

Otherwise, electron beam lithography (EBL)-assisted dry etching is another method. To achieve wafer-scale mass production, multi-step lithography processes based on EBL have become the preferred approach. EBL-based techniques rely on multistep protocols, akin to those implemented for silicon photonics or electronics (see sketch in Figure 1B). A typical process begins by realizing a hard mask on the wafer to be structured. A tightly focused electron beam is used to directly shape an electron-sensitive organic layer (resist), and in the next step, a lift-off process or reactive-ion etching (RIE) can be used to structure a hard mask. Finally, the pattern of the hard mask can be transferred to $LiNbO_3$ via ion-beam etching or RIE[67,78]. Because, except for the electron beam illumination, all these fabrication steps treat the entire wafer surface at once, EBL can process large sample areas up to several $cm^2$, which makes it more suitable for wafer-scale processing than FIB. The typical resolution achievable is ~20 nm, and the typical side-wall angle for small meta-atoms varies between 70° and 80°. Both parameters, as well as the surface roughness, limit the achievable Q-factor and strongly depend on the exact fabrication recipe. Therefore, to boost the quality of $LiNbO_3$ metasurfaces, further improvements in the fabrication techniques would be necessary.

### 2.2 Bottom-up

Alternatively to the methods based on thin films and deterministic structuring, single $LiNbO_3$ nanoparticles sustaining resonances can

also be fabricated through bottom-up approaches[79-82]. This can be achieved with laser ablation, but also several possibilities to produce (crystalline) particles with chemical synthesis were demonstrated, as sketched in Figure 1C, such as, molten salt syntheses[83,84] solution-phase synthesis with directed aggregation for controlled growth of crystalline $LiNbO_3$ nanostructures[85], synthesis of $LiNbO_3$ nanostructures with different morphologies from a single-source precursor by controlling the solvothermal conditions[86], and increased uniformity synthesis of single-crystalline $LiNbO_3$ nanoparticles by controlled Ostwald ripening[87]. Although these chemical methods can cost-effectively produce well-crystallized nanoparticles, they lack precision in controlling geometric morphology and size, particularly at scales above 100 nm. More critically, bottom-up approaches struggle to achieve deterministic arrangement of nanoparticles on substrates. For metasurface applications, precise control over the geometric dimensions of unit cells to tune resonance wavelengths, along with achieving periodic arrangements at subwavelength scales, is essential[88,89].

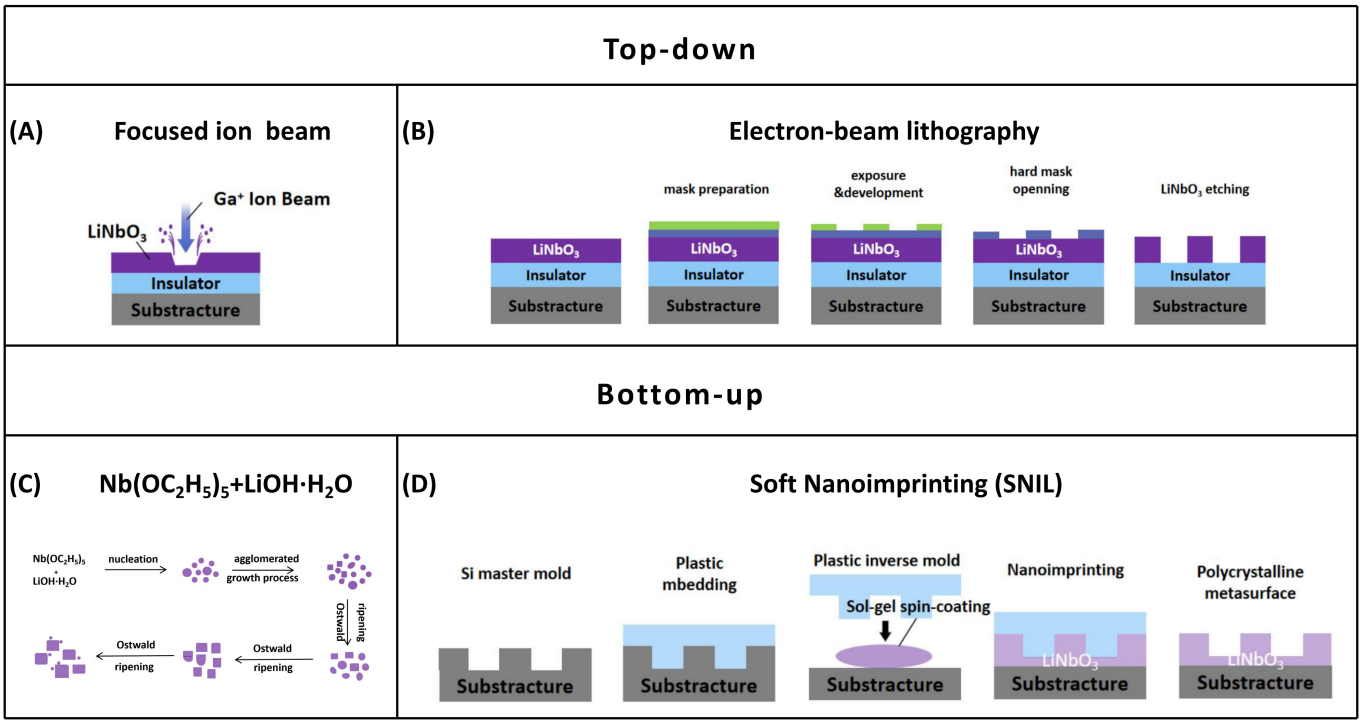


**Figure 1.** Overview of fabrication methods. (A-B) Top-down methods based on (A) FIB and (B) EBL; (C-D) Top-down methods based on (C) Sketch including the essential chemicals for solvothermal synthesis and (D) SNIL. FIB: focused ion beam; EBL: electron beam lithography; SNIL: soft nanoimprinting.

In 2025, Talts *et al.* proposed a direct soft nanoimprinting (SNIL) technique based on sol-gel precursors, as sketched in Figure 1D[90]. This method utilizes a poly(dimethylsiloxane) soft mold to directly replicate pre-designed metasurface patterns onto $LiNbO_3$ gel. After high-temperature annealing, it forms polycrystalline $LiNbO_3$ nanostructures. This "etch-free" process effectively avoids sidewall roughness and lattice damage caused by traditional dry etching, enabling the fabrication of photonic structures with an aspect ratio up to 6 and nearly vertical sidewalls.

## 3. $LiNbO_3$ Metasurfaces For Second-Order Up-Conversion

Having established the fabrication strategies for $LiNbO_3$ metasurfaces, we now turn to the optical functionalities that these carefully engineered nanostructures can unlock. SHG and its non-degenerate counterpart, SFG, are among the most fundamental second-order NLO effects. $LiNbO_3$ possesses a broad bandgap and high second-order NLO coefficients, enabling efficient nonlinear effects across a wide spectral range from UV to mid-infrared[41,91,92], including these second-order up-conversion processes. In $LiNbO_3$ platforms, the enhancement of SHG and SFG is predominantly achieved through resonant modulation of the local electromagnetic field. From the perspective of the underlying physical mechanism, existing $LiNbO_3$ photonic structures for nonlinear enhancement can be broadly categorized into two distinct classes. The first class relies on local resonance metasurfaces, where discrete optical modes confined within individual nanostructures, such as Mie-type resonances, toroidal dipole resonances, and anapole resonances, enable strong near-field confinement and energy accumulation within a subwavelength volume, thereby amplifying nonlinear light-matter interactions at the single-unit-cell level. The second class exploits nonlocal resonance metasurfaces, in which the optical response arises from collective interactions among multiple unit cells across the metasurface plane; radiative losses are suppressed through symmetry protection or interference effects within the radiation continuum, giving rise to ultra-high-Q-factor resonances such as BICs and GMRs. In the following, these two enhancement paradigms are discussed in detail. It is worth noting that while SHG

serves as the primary benchmark in the following subsections, it is fundamentally the degenerate case of SFG. Therefore, the resonance strategies discussed herein are physically applicable to both processes.

It is worth noting that the enhancement factors (EF) reported in various literature often rely on different reference baselines. In this review, unless otherwise specified, the EF for SHG is defined relative to an unpatterned TFLN of identical thickness under the same pump conditions. For studies that utilize different baselines (e.g., normalization against bulk $LiNbO_3$ or non-resonant nanostructures), specific distinctions are explicitly annotated in the text and comparison tables to ensure rigorous evaluation.

### 3.1 Localized-resonance $LiNbO_3$ photonic structures

Local resonances are primarily sustained by individual nanostructures, largely independent of the surrounding lattice periodicity. By supporting well-defined resonances in subwavelength-scale $LiNbO_3$ nanostructures or microcavities, these systems substantially increase the local field intensity inside the material, thereby amplifying second-order nonlinear processes such as SHG. However, they generally exhibit relatively low Q factors due to inherent radiative and non-radiative losses. Early research efforts were primarily directed toward the utilization of hybrid metal-dielectric structures to enhance SHG. For instance, a study on enhanced SHG in $LiNbO_3$ employed gold nanorings filled with $LiNbO_3$ that were fabricated on an $LiNbO_3$ substrate, as shown in Figure 2A. These nanoring structures were patterned onto monolithic x-cut $LiNbO_3$ substrates (where the crystalline Z-axis lies within the substrate plane), significantly enhancing SHG by exploiting plasmon-enhanced localized electromagnetic fields. Compared to unstructured substrates, a nearly 20-fold increase in SHG intensity was reported[92]. However, the intrinsic ohmic losses in metals restrict improvements in optical damage thresholds and conversion efficiencies, precipitating a shift toward all-dielectric $LiNbO_3$ metasurfaces as the dominant platform.

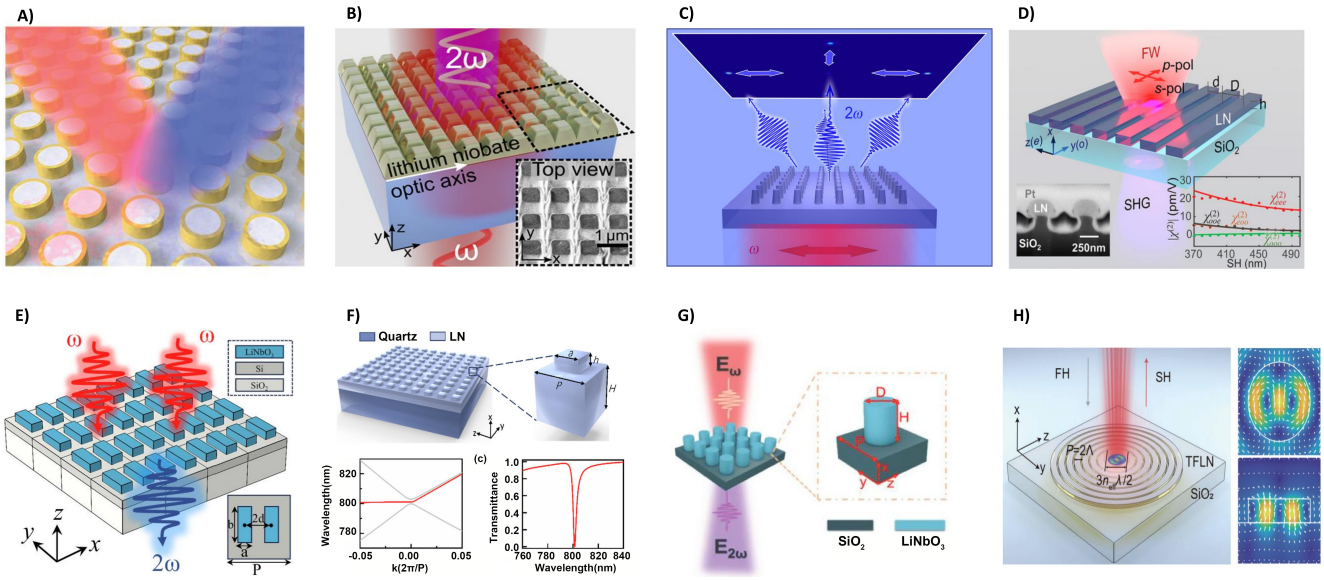


**Figure 2.** Resonance-enhanced $LiNbO_3$ metasurfaces for SHG. (A) Nonlinear metasurfaces based on gold Nanoring filled with $LiNbO_3$. Reproduced with permission from reference[92]. Copyright © 2015 American Chemical Society; (B) By nanostructuring thin x-cut $LiNbO_3$ film. Reproduced with permission from reference[67]. Copyright © 2020 American Chemical Society; (C) By nanostructuring a thick z-cut $LiNbO_3$ substrate. Reproduced from reference[68]. CC BY 4.0; (D) $LiNbO_3$-based 1D photonic grating. Reproduced with permission from reference[69]. Copyright © 2021 John Wiley & Sons; (E) $LiNbO_3$ metasurface composed of asymmetric nanobar pairs[61]. Adapted with permission from reference[61]. Copyright © 2024 Optica Publishing Group; (F) Shallow-etched $LiNbO_3$ unit on a quartz substrate. Adapted with permission from reference[60]. Copyright © 2025 Optica Publishing Group; (G) Anapole-resonant $LiNbO_3$ metasurface composed of nanodisks. Reproduced with permission from reference[94]. Copyright © 2024 John Wiley & Sons; (H) TFLN CBN. Reproduced with permission from reference[95]. Copyright © 2024 American Chemical Society. SHG: second harmonic generation; TFLN: thin-film lithium niobate; CBN: circular Bragg nanocavity.

Within the domain of all-dielectric systems, monolithic $LiNbO_3$ metasurfaces have been shown to exhibit highly efficient SHG governed predominantly by Mie-type resonances. Fedotova *et al.* reported resonant metasurfaces fabricated on x-cut TFLN. By tuning the nanopillar geometry to match the pump wavelength, the excitation of electric and magnetic dipole (MD) resonances was achieved at telecom wavelengths, as illustrated in Figure 2B. These resonant modes facilitate the tight confinement of electromagnetic fields within the nanopillars, thereby enhancing light-matter interactions; consequently, a significant resonant enhancement of SHG efficiency was observed compared to non-resonant structures, achieving a conversion efficiency in the order of $10^{-6}$[67]. Moreover, as shown in Figure 2C, the MD resonance exhibited a strong out-of-plane electric field component, thus maximizing access to the nonlinear $d_{33}$ component along the out-of-plane direction of z-cut $LiNbO_3$. This configuration allows for the encoding of the pump light's polarization into specific second harmonic (SH) polarization states and diffraction orders[68]. Similarly, this polarization control

was exploited in one-dimensional Mie-type nanogratings on x-cut TFLN, as shown in Figure 2D, which demonstrated spectrally tunable and highly polarized visible emission[69].

While fundamental Mie resonances offer significant improvements, their relatively broad linewidths (radiative losses) impose limits on field enhancement. To overcome this, high-Q modes such as magnetic toroidal dipole (MTD) resonances have been explored. As illustrated in Figure 2E, the metasurface is composed of an array of engineered $LiNbO_3$ nanostructures, designed to excite a specific resonance mode governed by a toroidal current distribution. Through the manipulation of these MTD resonances, radiation losses are effectively suppressed, resulting in intense electromagnetic field confinement within the nanostructures. This high-Q mode significantly prolongs the light-matter interaction time, thereby leading to a substantial enhancement in SHG efficiency[61]. Notably, the robustness of these toroidal modes also offers practical engineering benefits. A scheme for enhancing SHG utilizing toroidal dipole resonances in shallowly etched $LiNbO_3$ metasurfaces was demonstrated by Chang *et al.* As depicted in Figure 2F[60], by fabricating shallow nanopillar arrays on the $LiNbO_3$ surface, the technical challenges inherent to high-aspect-ratio nanostructuring are circumvented. Compared to unpatterned films, this shallowly etched architecture not only simplifies the fabrication protocol but also yields a substantial enhancement (approximately 10-fold) of the SHG signal, thereby offering promising avenues for the development of cost-effective, high-efficiency nonlinear devices.

To mitigate the radiative losses associated with conventional dipolar modes, non-radiating states, most notably anapole modes, have garnered significant attention. Anapole resonances originate from the destructive interference between electric and toroidal dipole moments (e.g., toroidal and electric dipoles), a mechanism that effectively suppresses far-field radiation while maximizing near-field confinement. In $LiNbO_3$ metasurfaces, the excitation of anapole resonances was theoretically proposed by exploiting the high refractive index contrast between $LiNbO_3$ nanodisks and low-index $SiO_2$ substrates[93]. When combined with the broad transparency window of $LiNbO_3$, this mechanism offers the potential to circumvent the absorption limitations of conventional materials, thereby enabling efficient SHG in the vacuum ultraviolet (VUV) band[94]. As illustrated in Figure 2G, the fabricated metasurface consists of an array of nanodisks patterned on TFLN. Theoretically, this unique “dark mode” facilitates the effective suppression of radiative scattering, resulting in the high confinement of electromagnetic energy within the nanodisks. Consequently, the extended photon lifetime directly translates to a remarkable enhancement in nonlinear conversion efficiency. Expanding beyond the anapole concept, recent work has incorporated more sophisticated interference mechanisms based on photonic crystal theories. For instance, a circular Bragg nanocavity architecture was proposed by Li *et al.* Fabricated on x-cut TFLN, the device comprises a central defect region circumscribed by periodic concentric ring gratings. By leveraging the radial Bragg reflection mechanism, the optical field is tightly confined within the central nanocavity, thereby establishing a high-Q resonant anapole-like cavity mode. Notably, this photonic crystal nanocavity platform achieves one of the highest SHG enhancement factors reported for TFLN nanostructures to date, reaching approximately $4.2 \times 10^4$, as shown in Figure 2H[95].

### 3.2 Nonlocal-resonance $LiNbO_3$ photonic structures

In contrast to localized modes, nonlocal resonances arise from the collective interplay and coherent coupling across the periodic metasurface lattice. In this approach, optical modes are not isolated from free-space radiation by geometric confinement, but instead remain embedded within the continuum and become localized through symmetry protection or destructive interference among multiple radiation channels. This class of structures includes BICs and closely related GMRs in periodic $LiNbO_3$ platforms. Unlike conventional localized Mie-type resonances, nonlocal mechanisms inherently suppress radiative leakage through the collective interplay of the periodic lattice. Specifically, by engineering continuum modes or introducing symmetry-breaking perturbations, perfectly dark states are transformed into quasi-BICs. This precise structural tuning enables efficient external pump coupling while maintaining exceptionally high Q factors. Consequently, they offer an unprecedented platform for dramatically boosting SHG conversion efficiency over macroscopic areas.

#### 3.2.1 Etched $LiNbO_3$ metasurfaces

As an early representative example, efficient SHG in $LiNbO_3$ metasurfaces governed by quasi-BICs modes was numerically demonstrated in Figure 3A[96]. This high Q factor quasi-BICs resonance facilitated extreme energy confinement within the resonator volume, yielding a field enhancement factor exceeding 190. Numerical results indicated that, utilizing a high Q-factor of $8 \times 10^4$, a peak SH conversion efficiency of 0.49% was achieved at a relatively low pump intensity of 3.3 kW/cm$^2$. Beyond structural asymmetry, off-normal incidence and material anisotropy provide additional routes for BICs excitation. To address the challenge of utilizing the maximum nonlinear coefficient ($d_{33}$) of z-cut TFLN under normal incidence, a two-dimensional nanocone array supporting quasi-BICs modes was proposed, as depicted in Figure 3B. By breaking the symmetry protection by off-normal incidence (finite in-plane wavevector), quasi-BICs modes featuring strong longitudinal electric field components ($E_z$) were excited. Experimental observations revealed that an SHG enhancement of over 400-fold relative to unpatterned films was achieved[97]. Furthermore, as illustrated in Figure 3C, a quasi-BICs metasurface exploiting the anisotropic properties of $LiNbO_3$ was proposed. In contrast to isotropic structures, the birefringence of $LiNbO_3$ induces the splitting of the originally degenerate BICs mode into two high-Q quasi-BICs modes featuring orthogonally polarized responses. This physical mechanism enables the selective excitation of specific resonant modes by altering the pump polarization, thereby achieving precise manipulation of the localized optical field[98].

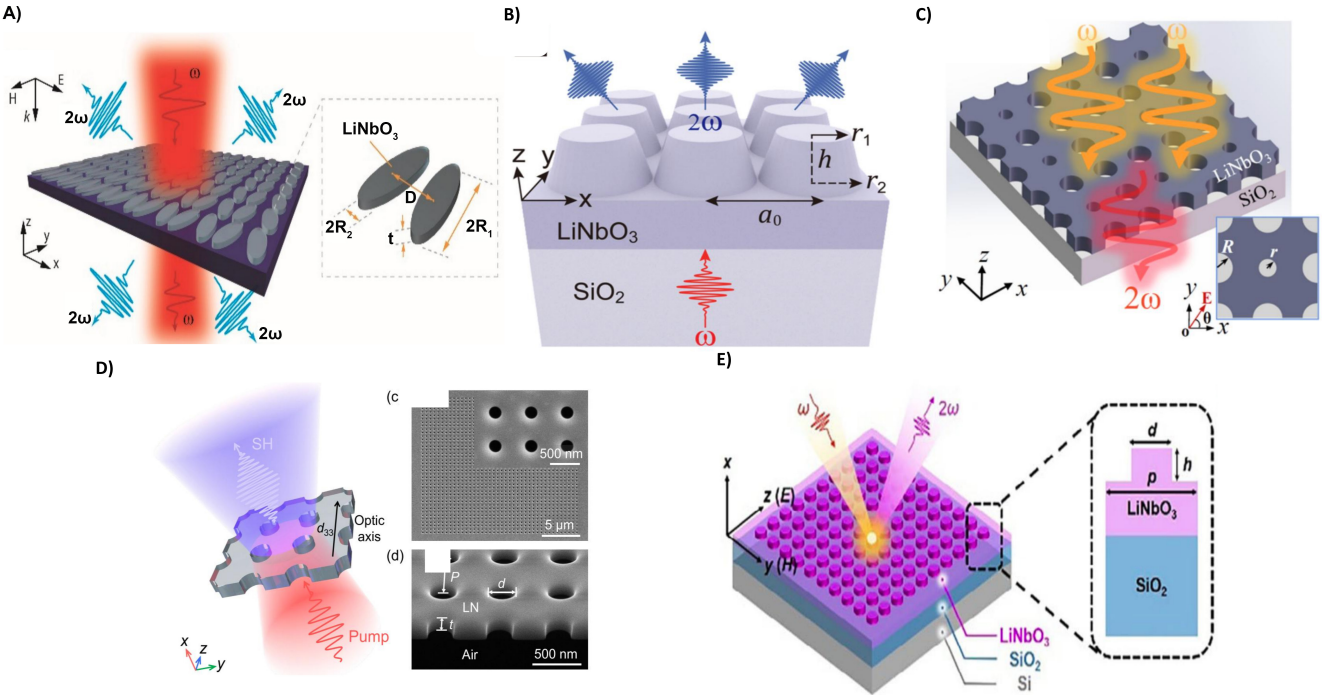


**Figure 3.** Continuum-engineered metasurfaces based on $LiNbO_3$ for SHG enhancement. (A) Asymmetric $LiNbO_3$ metasurface composed of nanobar pairs. Adapted with permission from reference[96]. Copyright © 2021 Optica Publishing Group; (B) Quasi-BICs resonant z-cut $LiNbO_3$ metasurface composed of truncated nanocones. Reproduced with permission from reference[97]. Copyright © 2022 John Wiley & Sons; (C) Quasi-BICs resonant anisotropic $LiNbO_3$ metasurface composed of composite nanoholes. Adapted with permission from reference[98]. Copyright © 2023 Optica Publishing Group; (D) Freestanding x-cut $LiNbO_3$ membrane metasurface composed of a square lattice of circular air holes. Reproduced with permission from reference[99]. Copyright © 2022 American Chemical Society; (E) Coupled GMRs x-cut $LiNbO_3$ metasurface composed of a square lattice of shallow-etched nanodisks. Reproduced with permission from reference[102]. Copyright © 2025 John Wiley & Sons. SHG: second harmonic generation; BICs: bound states in the continuum; GMRs: guided-mode resonances.

To address the field confinement bottleneck arising from the low refractive index contrast in conventional substrate-supported structures, a $LiNbO_3$ metasurface based on a freestanding membrane architecture was developed, as depicted in Figure 3D[99]. This freestanding configuration provides an exceptionally large refractive index contrast in the vertical direction, which significantly suppresses radiative leakage of slab waveguide modes and enables the excitation of GMRs. Experimental results demonstrate that a second-harmonic conversion efficiency as high as $2.0\times10^{-4}$ was achieved. Complementary to manipulating vertical confinement, engineering in-plane feedback is equally crucial for optimizing GMRs cavities. As a compelling example, Yuan *et al.* elegantly demonstrated strongly enhanced SHG by employing a one-dimensional GMRs heterostructure cavity on a TFLN platform. By combining a central grating coupler with side distributed Bragg reflectors, this structural engineering effectively suppresses in-plane radiation, achieving a high Q-factor of over 5,000 and a 1,200-fold SHG enhancement relative to unpatterned films[100]. Then, extending the scope of continuum engineering beyond fundamental SHG efficiency, Zhao *et al.* demonstrated the capability of GMRs to tackle the challenges of HHG. Benefiting from resonance-enhanced localized optical fields and nanoscale interaction lengths, a normalized second-harmonic conversion efficiency of $5.1 \times 10^{-5}$ $cm^2$ $GW^{-1}$ was achieved[101]. Furthermore, a breakthrough in the deep ultraviolet (DUV) band was realized, where harmonic generation up to the seventh order was experimentally observed, extending the nonlinear radiation wavelength down to 226 nm. As shown in Figure 3E, by precisely tuning the coupling strength between two spectrally adjacent GMRs modes, high-Q-factor resonances exhibiting exceptionally strong field localization were excited. Experimental results demonstrated that owing to the effective confinement of the optical field by the coupled GMRs, an absolute second-harmonic conversion efficiency on the order of $10^{-3}$ was achieved in the near-UV band (~395 nm)[102].

### 3.2.2 Hybrid $LiNbO_3$ metasurfaces

Although the modal energy of an ideal BICs lies within the radiation continuum, radiation leakage can be strongly suppressed through symmetry protection or destructive interference, resulting in ultranarrow linewidths and exceptionally high Q factors. However, such radiation suppression relies on precise structural conditions and is therefore highly vulnerable to fabrication-induced perturbations. In practical nanostructures, the sidewalls are rarely perfectly smooth, vertical, and sharply defined; instead, imperfections such as edge jaggedness, local tilt, and boundary fluctuations are commonly present after fabrication. These nonideal features break the symmetries required for BICs formation and introduce random structural disorder, thereby opening parasitic radiation channels and enhancing scattering loss. The total Q factor can generally be expressed as:

$$\frac{1}{Q_{tot}} = \frac{1}{Q_{rad}} + \frac{1}{Q_{mat}} + \frac{1}{Q_{scat}} \quad (1)$$

where $Q_{rad}$ denotes the radiative quality factor associated with energy leakage into the far field, $Q_{mat}$ represents material-related losses such as intrinsic absorption in the dielectric medium, and $Q_{scat}$ accounts for scattering losses induced by structural imperfections, including sidewall roughness and fabrication-induced disorder. For BICs or quasi-BICs resonances, $Q_{rad}$ is intentionally enhanced through radiation suppression, while material absorption in $LiNbO_3$ is usually relatively weak. Under these conditions, scattering loss associated with sidewall roughness can become the dominant limiting factor for the overall $Q_{tot}$. This sensitivity is much stronger than that of conventional Mie-type resonances, which typically exhibit broader linewidths and are therefore less susceptible to small structural perturbations.

Owing to this strong dependence on scattering-induced loss, BICs and quasi-BICs resonances are intrinsically sensitive to fabrication-induced imperfections. Consequently, the experimentally achievable Q factor of BICs metasurfaces is often strongly dependent on the fabrication method and the resulting structural fidelity. In practice, several nanofabrication techniques have been employed for the realization of BICs metasurfaces, and each of them imposes distinct constraints on the attainable sidewall quality, dimensional accuracy, uniformity, and scalability. FIB milling offers high patterning resolution and design flexibility, but may introduce ion-induced damage and redeposition effects that degrade sidewall smoothness and structural consistency. Dry etching approaches, such as RIE, are more suitable for scalable and large-area fabrication, yet their performance remains highly sensitive to etching conditions, which directly affect sidewall morphology and profile fidelity. Wet etching, by contrast, is generally limited by its isotropic nature and is therefore less favorable for the fabrication of high-Q BICs nanostructures requiring sharp and vertical sidewalls. These fabrication-related trade-offs are often reflected in reduced Q factors, resonance broadening, and device-to-device variability in experimentally realized BICs metasurfaces.

In this context, etch-free or low-damage fabrication strategies have attracted increasing attention as promising alternatives for mitigating roughness-induced degradation and better preserving the intrinsic high-Q characteristics of BICs resonances. As a representative implementation utilizing low-refractive-index dielectrics, a hybrid heteronanostructure comprising a $SiO_2$ photonic crystal slab integrated atop an x-cut TFLN was demonstrated[103]. Experimental results demonstrated that a high-Q resonance (Q factor $\approx$ 980) was excited within this heterostructure, resulting in an SHG signal enhancement of approximately 1,500-fold relative to unpatterned films. Notably, efficient nonlinear conversion was achieved at relatively low pump intensities (approximately 45 MW/cm$^2$). Beyond standard inorganic dielectrics, polymers have also been introduced into heterogenous integration. As shown in Figure 4A, distinct from single-mode excitation, a polymer-$LiNbO_3$ integrated metasurface was developed to support the coexistence of multiple high-Q optical resonances, arising from the interplay between polymer-induced lattice/Mie resonances and waveguiding effects in $LiNbO_3$. Experimental results demonstrated that all four supported modes exhibit Q-factors exceeding 1,000[104]. To further extend the spectral operating range and enhance tunability, nonlocal metasurfaces employing high-refractive-index dielectrics have been explored. Figure 4B depicts such a design, integrating a period-doubling $TiO_2$ grating onto a TFLN[105]. Through the introduction of geometric perturbations, guided modes originally confined below the light line are folded into the radiative continuum, transforming them into highly robust quasi-GMs. These modes effectively maintain high-Q resonances across a broad spectral range, enabling wavelength selection via incident angle adjustment to achieve spectrally tunable SHG.

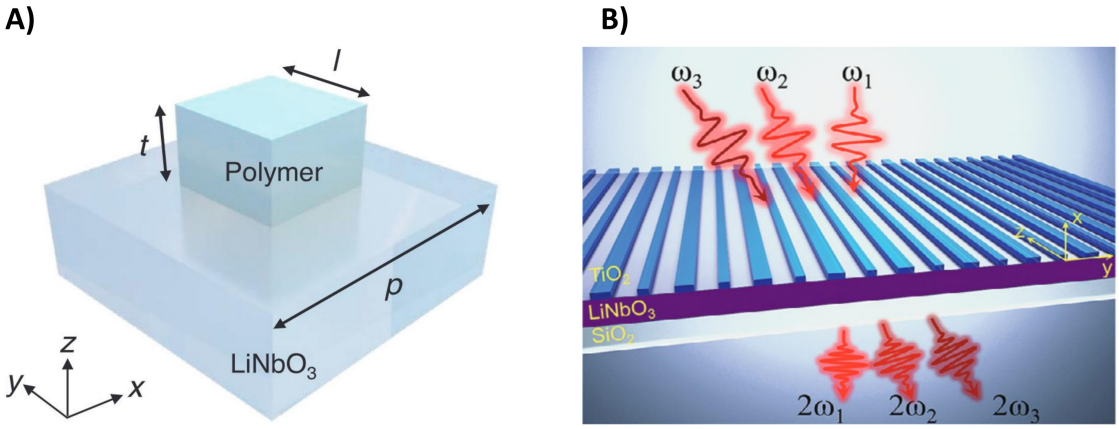


**Figure 4.** Hybrid unetched $LiNbO_3$ metasurfaces for SHG. (A) A polymer-$LiNbO_3$ integrated metasurface. Reproduced with permission from reference[104]. Copyright © 2023 John Wiley & Sons; (B) Tunable SHG in a nonlocal metasurface over a broad spectral range. Reproduced with permission from reference[105]. Copyright © 2024 John Wiley & Sons. SHG: second harmonic generation.

Furthermore, leveraging the angular dispersion inherent to such non-localized resonances also opens the door to two-beam SHG (or non-collinear SHG), where two pump beams intersect within the metasurface. This vectorial wave-mixing process serves as a perfect

conceptual and geometric bridge to non-degenerate SFG. Unlike degenerate SHG, SFG offers the critical advantage of mixing two distinct driving frequencies, thereby enabling highly flexible spectral tunability. This tunability is particularly desirable for up-conversion imaging. For instance, recent advancements have demonstrated highly efficient SFG in $LiNbO_3$ metasurfaces, showcasing the ability to up-convert infrared signals into the visible spectrum with high spatial resolution and enhanced nonlinear overlap[106].

### 3.3 Analysis of efficiency variations in $LiNbO_3$ metasurfaces

The reported SHG conversion efficiencies in $LiNbO_3$ metasurfaces exhibit a significant spread, typically ranging from $10^{-6}$ to $10^{-3}$ (Table 2). This three-order-of-magnitude variation can be systematically understood through the fundamental scaling law governing nonlinear light-matter interactions.

**Table 2.** SHG performances of selected $LiNbO_3$ metasurfaces.

| Reference | Material cut | Resonance type | Q-factor | SHG efficiency/Enhancement |
|---|---|---|---|---|
| Lehr *et al.*[92] | X cut | plasmonic resonance | - | 18 (Exp.)<br>23 (Sim.) |
| Fedotova *et al.*[67] | X cut | Mie-type resonances | - | $10^{-6}$ |
| Carletti *et al.*[68] | Z cut | Mie-type resonances | ~10 | $2.5 \times 10^{-8}$ |
| Ma *et al.*[69] | X cut | Mie-type resonances | - | $2 \times 10^{-6}$ |
| Duan *et al.*[61] (only numerical) | X cut | MTD | $10^{10}$ | $1.15 \times 10^{-2}$ |
| Chang *et al.*[60] | X cut | Toroidal Dipole | 104 (Exp.),<br>262 (Sim.) | 10 |
| Liu *et al.*[94] | X cut | Anapole resonance | - | 30 |
| Li *et al.*[95] | X cut | Anapole; (CBN) | 260 | 42,000 |
| Kang *et al.*[96] (only numerical) | X cut | Quasi-BICs | $8 \times 10^4$ | $4.9 \times 10^{-3}$ |
| Zhang *et al.*[97] | Z cut | Quasi-BICs | > 1,000 | 400 |
| Huang *et al.*[103] | X cut | Quasi-BICs | 980 | $6.87 \times 10^{-7}$ |
| Liu & Zhou[98] (only numerical) | X cut | Quasi-BICs | $\infty$ | $6.04 \times 10^{-3}$ |
| Yuan *et al.*[100] | X cut | GMRsheterostructure cavity | > 5,000 (max),~2,000 (optimal) | $2.03 \times 10^{-5}$ |
| Qu *et al.*[99] | X cut | GMRs | 75 | $2 \times 10^{-4}$ |
| Zhao *et al.*[101] | X cut | GMRs | - | $8.6 \times 10^{-3}$ |
| Fang *et al.*[104] | X cut | Quasi-GMs | 1,028 | 25.4 |
| Jiang *et al.*[105] | X cut | Quasi-GMs | 2,697 | 1,200 |
| Wang *et al.*[102] | X cut | GMRs | 420 (exp.),<br>$10^4$ (sim.) | $1.36 \times 10^{-3}$ |

SHG: second harmonic generation; MTD: magnetic toroidal dipole; CBN: circular Bragg nanocavity; BICs: bound states in the continuum; GMRs: guided-mode resonances; GMs: guided modes.

$$\eta \propto \left( \frac{Q_\omega^2 \cdot Q_{2\omega}}{V_{\text{eff}}} \right) \cdot \beta^2 \tag{2}$$

First, the most decisive factor is the leap in Q. Early designs primarily utilized Mie-type resonances with relatively high radiative losses, resulting in modest Q values ($10^1$–$10^2$) and efficiencies in the $10^{-6}$ regime. In contrast, the adoption of continuum-engineered resonances, such as BICs and GMRs, has enabled Q factors exceeding $10^3$–$10^5$. Given that the efficiency scales quadratically with Q at

the fundamental frequency, this enhancement in photon lifetime directly accounts for the bulk of the efficiency leap. Second, the effective mode volume ($V_{eff}$) has been significantly reduced through the development of freestanding membrane architectures and high-refractive-index-contrast gratings, which provide stronger electromagnetic field localization within the nonlinear medium. Finally, the spatial overlap integral (β), which quantifies the coupling between the resonant optical modes and the $LiNbO_3$ nonlinear susceptibility tensor, plays a critical role. Recent high-efficiency studies ($10^{-3}$ regime) specifically optimize the mode symmetry to maximize access to the $d_{33}$ coefficient of $LiNbO_3$. The evolution from simple resonant scattering to sophisticated mode-matching and light-trapping strategies underlies the dramatic performance improvements observed in recent years. Building upon the understanding of resonant enhancement, Lin *et al.* challenged the conventional reliance on high Q-factors as the sole predictor of nonlinear efficiency. By fabricating $LiNbO_3$ metasurfaces with controlled geometric parameters, they isolated the influence of electromagnetic field distribution under nearly identical Q-factors at the fundamental-frequency resonance. The study introduced and verified the mode overlap factor (β), demonstrating that even with identical Q-factors, the SHG efficiency varies drastically depending on how well the optical field is confined within the nonlinear material volume. This work establishes the product of Q and β as a more accurate figure of merit, shifting the design paradigm from simply maximizing resonances to optimizing the spatial overlap between the fundamental field and the material's nonlinear susceptibility[107].

### 3.4 Comparison and selection of resonance mechanisms

As discussed in the preceding sections, the various resonance and continuum-engineered mechanisms offer distinct pathways to enhance SHG in $LiNbO_3$ metasurfaces. However, they exhibit significant trade-offs between optical performance, fabrication complexity, and spectral applicability. To provide a systematic guideline, we summarize the key metrics of these mechanisms in Table 3.

**Table 3.** Comparison of physical mechanisms: Mie resonances, BICs, and GMRs.

| Mechanism | Physical origin | Advantages | Limitations | Scenarios |
|---|---|---|---|---|
| Mie Resonances | Multipolar excitations (electric/magnetic) in high-index subwavelength particles. | Strong subwavelength localization; versatile phase/amplitude control; supports Huygens' sources. | Relatively low Q factors (typically < 100); significant radiative loss. | Metalenses, holography, structural color, and beam steering. |
| BICs (quasi-BICs) | Suppression of radiation via symmetry breaking or interference between modes. | Extremely high Q-factors; massive near-field enhancement; ultra-narrow resonance linewidth. | Highly sensitive to fabrication tolerances and symmetry-breaking geometry; narrow operational bandwidth. | Nano-lasers, nonlinear harmonic generation, and ultra-sensitive bio-sensing. |
| GMRs | Phase-matching between incident light and leaky waveguide modes, facilitated by periodic structures (or gratings). | High efficiency (near 100%); flexible spectral tuning over wide ranges; easier large-area fabrication. | Highly sensitive to the angle of incidence; performance depends on the cladding/substrate interface. | Narrow-band filters, refractive index sensors, and polarization beam splitters. |

BICs: bound states in the continuum; GMRs: guided-mode resonances.

For applications prioritizing broad spectral operation, polarization control, and high fabrication tolerance, discrete Mie resonances and shallow-etched toroidal dipoles are highly favorable. Their relatively simple geometries circumvent the severe challenges of high-aspect-ratio $LiNbO_3$ dry etching. Conversely, for processes demanding extreme nonlinear conversion efficiencies or operation in challenging spectral regimes (such as the DUV or VUV bands), continuum-engineered modes like quasi-BICs and GMRs, as well as anapole modes, become indispensable. These mechanisms can achieve ultra-high Q-factors and record-high field enhancements.

Nevertheless, the implementation of ultra-high-Q resonances introduces a strict bottleneck regarding fabrication complexity. Modes such as quasi-BICs are notoriously sensitive to symmetry-breaking imperfections and sidewall roughness, which can easily open unwanted radiation channels and degrade the Q-factor. To mitigate this, hybrid "unetched" strategies employing secondary materials (e.g., $SiO_2$, polymers, or $TiO_2$) have proven to be a robust alternative, transferring the fabrication burden away from the chemically inert $LiNbO_3$. Ultimately, as highlighted by the introduction of the mode overlap factor (β), the optimal selection of a resonance mechanism should not blindly pursue the highest theoretical Q-factor. Instead, researchers must strike a delicate balance between minimizing radiative losses (high Q), maximizing the spatial overlap of the fundamental field with the nonlinear material (high β), and maintaining realistic fabrication tolerances.

## 4. Emerging Nonlinear Processes in $LiNbO_3$ Metasurfaces

While the second-order up-conversion processes (i.e., SHG and SFG) discussed in Section 3 serve as the foundational benchmarks for evaluating the nonlinear performance of $LiNbO_3$ metasurfaces, the potential of this platform extends far beyond frequency addition. Recent research frontiers have increasingly shifted toward other complex parametric and higher-order multiphoton processes, including DFG, SPDC, and HHG. Expanding metasurface designs to accommodate these phenomena is critical for the development of fully integrated classical and quantum photonic systems.

### 4.1 DFG

In contrast to the up-conversion mechanisms of SHG and SFG, DFG and its degenerate counterpart, optical rectification, provide a robust paradigm for extending the emission spectrum into the mid-infrared and THz regimes. A prominent challenge in realizing these processes lies in the severe fabrication constraints associated with directly nanostructuring $LiNbO_3$. To circumvent this, innovative hybrid architectures have been developed, such as integrating symmetry-broken all-dielectric metasurfaces (e.g., $SiO_2$) atop unpatterned TFLN[108]. By engineering high-Q quasi-BICs modes within the linear metasurface, the near-infrared pump fields are tightly localized and resonantly coupled into the underlying highly nonlinear substrate. This precise structural tailoring not only circumvents etching-induced lattice damage but also drastically amplifies the broadband THz emission, paving the way for ultra-compact, room-temperature coherent sources crucial for advanced spectroscopy and sensing.

### 4.2 SPDC

Beyond classical nonlinear wave mixing, $LiNbO_3$ metasurfaces are emerging as a pivotal platform for integrated quantum optics, primarily driven by the SPDC process. SPDC is a cornerstone mechanism for generating entangled photon pairs. By structuring $LiNbO_3$ at the subwavelength scale, researchers can effectively manipulate the emission directionality, polarization state, and generation rate of the photon pairs. For instance, an important advancement involved the demonstration of SPDC in resonant $LiNbO_3$ metasurfaces, as illustrated in Figure 5A[109]. By leveraging electric Mie-like resonances, researchers enhanced the photon-pair generation rate by over two orders of magnitude compared to unpatterned films, while successfully tailoring the emission spectrum through resonance detuning. Building upon such resonant architectures, subsequent breakthrough studies have realized highly directional and tunable entangled photon emission directly from ultra-thin $LiNbO_3$ metasurfaces, as illustrated in Figure 5B[110]. To further overcome the interaction volume limits in thin films, sophisticated resonant cavity designs have been employed. By harnessing high-Q nonlocal resonances, researchers have significantly boosted the generation rate and tailored the spectral properties of the SPDC biphotons[111]. These pioneering works effectively bridge the gap between nonlinear flat optics and highly integrated quantum information technologies, marking a vital direction for future research.

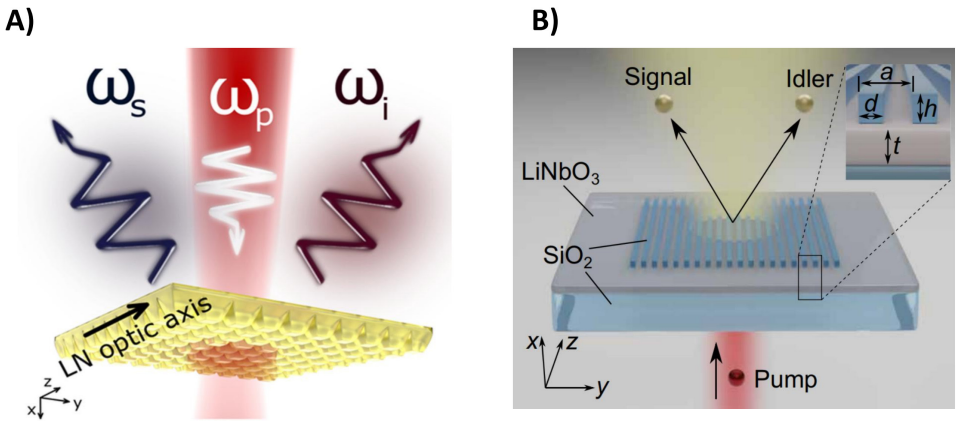


**Figure 5.** $LiNbO_3$ metasurfaces for other nonlinear processes. (A) Scheme of SPDC generation in reflection by a $LiNbO_3$ metasurface. Reproduced from reference[109]. CC BY 4.0; (B) Scheme of SPDC by an etchless metasurface on thin-film $LiNbO_3$. Reproduced from reference[110]. CC BY 4.0. SPDC: spontaneous parametric down-conversion.

### 4.3 HHG

Pushing the boundaries of nonlinear optics, HHG in solid-state materials enables the generation of coherent DUV or extreme-ultraviolet (EUV) radiation. As introduced earlier in Section 3.2, preliminary breakthroughs have successfully utilized GMRs in $LiNbO_3$ metasurfaces to alleviate above-gap absorption, achieving HHG up to the 7th order (down to 226 nm)[101]. Moving forward, the critical challenge for advancing HHG toward practical applications is twofold. First, the material must withstand the extreme optical pump intensities required for higher-order multiphoton processes without suffering from optical damage or photothermal degradation. Second, the nanostructures must be meticulously engineered to efficiently extract the generated DUV/EUV photons to the far-field before they are reabsorbed by the material's intrinsic interband transitions. Overcoming these fundamental extraction and damage-threshold limits will be pivotal for developing compact, chip-scale coherent DUV light sources.

## 5. $LiNbO_3$ Metasurfaces For Phase Modulation

Beyond NLO enhancement, $LiNbO_3$ metasurfaces also offer powerful capabilities for wavefront manipulation through static phase modulation. While the resonance engineering discussed in Section 3 primarily targets intensity enhancement, precise control over the phase of scattered light opens a new dimension for flat-optics applications. In this section, we discuss two fundamental phase modulation mechanisms (resonant phase and PB phase), and examine how they are implemented in $LiNbO_3$ metasurface designs. Early metasurface research established generalized Snell's law, revealing the fundamental principle of controlling light propagation through phase discontinuities at interfaces[14]. Subsequently, various phase-modulation mechanisms have been extensively studied and summarized in both dielectric and metallic metasurfaces[1,112,113]. In the context of $LiNbO_3$ metasurfaces, phase manipulation is predominantly realized through two mechanisms: geometric phase (PB phase) introduced by in-plane rotation of anisotropic meta-atoms, and resonant phase arising from mode interference in engineered resonant structures.

### 5.1 Resonance phase

Resonant phase modulation is primarily realized through the excitation of Mie resonances, BICs, or Fabry-Pérot cavity resonances within nanostructures. In the vicinity of the resonance frequency, an abrupt phase variation is induced in the optical field, typically spanning a range of 0-π or 0-2π. This mechanism is inherently accompanied by substantial local field enhancement, rendering it particularly advantageous for the simultaneous enhancement of nonlinear conversion efficiency and the wavefront shaping of the generated nonlinear signal.

To address the limitations of existing UV nonlinear metalenses, specifically the low nonlinear susceptibility of conventional materials and fabrication constraints, a $LiNbO_3$ nonlinear metalens was developed, as illustrated in Figure 6[114]. This research employed a self-developed multi-atmosphere cooperative etching technique to fabricate elliptical nanohole arrays with steep sidewalls and smooth surfaces on x-cut TFLN. By precisely tuning the GMRs at the fundamental wavelength within the nanohole structure, the device achieved full phase coverage from 0 to 2π for the second-harmonic wave while simultaneously amplifying the localized optical field. Experimental results demonstrated that this metalens successfully converts and focuses 780 nm fundamental light into 390 nm UV second-harmonic light, achieving a numerical aperture (NA) of 0.7 and a near-diffraction-limited focal spot of 0.7 μm. Benefiting from the superposition of resonance enhancement and spatial focusing effects, the second-harmonic peak intensity at the focal point was amplified by 40-fold relative to the average intensity across the focal plane.

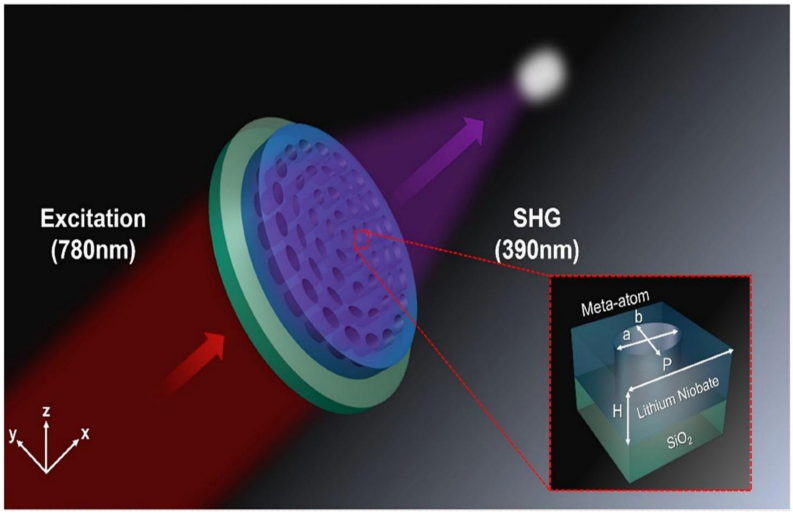


**Figure 6.** A $LiNbO_3$ nonlinear metalens based on resonant wavefront. Reproduced with permission from reference[114]. Copyright © 2025 American Chemical Society. SHG: second harmonic generation.

To further extend resonant phase modulation toward spectral-selective wavefront control, a TFLN metasurface was developed. This work employed two regions of nanostructures with distinct geometries to engineer spectrally tunable Mie-type resonances, thereby introducing a controllable phase difference in the second-harmonic field. By designing the resonances to occur exclusively at the second-harmonic wavelength while avoiding the fundamental wavelength, the device enables selective phase modulation of the nonlinear signal without disturbing the pump beam. Experimental results demonstrated that a Gaussian pump beam in the range of 1,000-1,300 nm can be converted into a structured second-harmonic beam at ~550 nm, exhibiting a first-order Hermite-Gaussian ($HG_{01}$) mode. The optimal mode conversion occurs near pump wavelengths of 1,100-1,200 nm, where the phase difference approaches ~π. This work highlights that resonant $LiNbO_3$ metasurfaces can achieve wavelength-selective nonlinear wavefront shaping, providing an additional degree of freedom beyond conventional geometric-phase-based designs[115].

### 5.2 PB phase

The PB phase, also known as the geometric phase, originates from the in-plane spatial orientation of anisotropic nanostructures. Upon the interaction of circularly polarized light with anisotropic meta-atoms acting as local half-wave plates with an orientation angle θ, a geometric phase shift of 2σθ is imparted to the cross-polarized component. By virtue of its non-dispersive nature and sole dependence on geometric orientation, the PB phase has been established as the preferred mechanism for realizing broadband wavefront modulation.

To address the fabrication challenges of monocrystalline $LiNbO_3$, specifically the difficulty in achieving high-aspect-ratio nanostructures due to chemical inertness, a polycrystalline $LiNbO_3$ nonlinear metalens was developed[90]. This research employed a scalable direct SNIL technique to fabricate triangular nanoprism arrays with nearly vertical sidewalls and aspect ratios of up to 6 using a novel solution-derived sol-gel material. By utilizing the geometric phase induced by the rotation of C3-symmetric meta-atoms, the device achieved broadband nonlinear wavefront control without relying on narrow-band resonances. Experimental results demonstrated that this metalens successfully converts and focuses fundamental light across a broad range (760-1,550 nm) into near-UV to near-infrared second-harmonic light, achieving a NA of 0.16 and a focal spot size of 1,050 nm at 400 nm wavelength. Benefiting from the high effective second-order nonlinearity of the polycrystalline material ($d_{eff} \approx 4.8$ pm/V) and efficient spatial focusing, the second-harmonic signal intensity at the focal point was amplified by up to 34-fold relative to the unshaped emission at the metalens surface.

## 6. Dynamic Adjustment $LiNbO_3$ Metasurfaces

The static phase modulation strategies described in Section 5 enable versatile wavefront control; however, they lack the ability to reconfigure optical responses after fabrication. To overcome this limitation, the strong EO effect intrinsic to $LiNbO_3$ provides a compelling route toward dynamic and high-speed tunability. In this section, we focus on EO tuning strategies, including EO phase modulation and EO resonance tuning, which together enable active, real-time control of the metasurface optical response. To bridge the gap toward adaptive optical systems, the development of mechanisms to actively modulate metasurface characteristics is essential[116]. Consequently, the dynamic control of optical properties has emerged as a central frontier in nanophotonics[117]. Various tuning mechanisms have matured in recent years, including optical pumping[118], thermal heating[119], chemical reactions[120], and electrical stimulation[89]. Among all these control mechanisms, $LiNbO_3$ emerges as an ideal platform for realizing integrated, low-power dynamic photonic devices. This is due to its intrinsic thermo-optic and EO/Pockels effects, combined with the enhanced light-matter interactions enabled by metasurfaces. In particular, electric field control technology has garnered significant attention for its potential to seamlessly integrate metasurfaces with other on-chip optoelectronic devices[121].

EO modulation based on the linear Pockels effect offers the distinct advantages of low power consumption and ultrafast response speeds, extending into the GHz or even THz regimes. Consequently, this mechanism serves as a cornerstone technology for the realization of high-speed modulators, LiDAR systems, and dynamic holography. This second-order nonlinear process is characterized by a modification of the refractive index induced by an applied electrostatic or low-frequency electric field. The resulting refractive index modulation exhibits a linear dependence on the magnitude of the applied electric field. This effect is maximized when the direction of the electric field is parallel to the crystallographic c-axis. For small perturbations, the refractive index changes for the extraordinary ($n_e$) and ordinary ($n_o$) waves can be approximated as follows:

$$\Delta n_e \approx -\frac{1}{2} n_e^3 r_{33} E_z \text{ and } \Delta n_o \approx -\frac{1}{2} n_o^3 r_{13} E_z \tag{3}$$

Here, $E_z$ denotes the magnitude of the externally applied electric field, while $r_{33} \approx 31$ pm/V and $r_{13} \approx 8$ pm/V are the corresponding EO coefficients (typically cited at visible to near-infrared wavelengths).

So far, the EO effect has been investigated theoretically and experimentally in either one-dimensional[70,71] or two-dimensional[72,122] metasurfaces. The performances reported in these works are summarized in Table 4. All these realizations are based on TFLN where the modulating electric field produced by two planar electrodes lies in the metasurface plane and exploits the $r_{33}$ element, which is the largest. To overcome the intrinsically weak refractive index modulation described above, resonant enhancement strategies have been widely adopted to amplify the phase modulation sensitivity. Early efforts focused on establishing the fundamental link between resonant modes and dynamic phase control. In one representative study, the dynamic modulation of beam deflection was explored using resonant EO phase-gradient metasurfaces[71]. By exciting high-Q GMRs in silicon-on-$LiNbO_3$ nanobars, the induced refractive index change was effectively translated into a dynamic phase gradient, enabling tunable beam steering. Concurrently, experimental validation of this resonant phase enhancement was achieved. By utilizing oblique incidence to excite quasi-BICs, an experimental phase modulation amplitude of 0.0041 rad was achieved, under a driving voltage of 300 $V_{pp}$[70].

Building on these foundations, the focus shifted toward optimizing the “Phase-Voltage” relationship, aiming to achieve larger phase shifts at lower driving voltages by exploiting sharper resonances. A low-voltage phase modulation scheme based on structural asymmetry-induced quasi-BICs was proposed[123]. The core mechanism here relies on the steep phase dispersion associated with

high-Q resonances, which allows for significant phase tuning with minimal voltage changes. In parallel, to leverage the mature fabrication technology of silicon while harnessing the strong Pockels effect of $LiNbO_3$, a high-Q-factor silicon-on-$LiNbO_3$ metasurface was proposed and numerically investigated, as depicted in Figure 7A[124]. In this work, Klopfer *et al.* utilized engineered periodic notches in silicon-on-TFLN gratings to excite ultra-sharp GMRs (Q > 30,000). This high-Q design theoretically enables a full 2π phase tuning range under a bias of only ± 25 V without requiring complex $LiNbO_3$ etching, with efficiencies as high as 86%, establishing a practical route for reconfigurable phase masks.

**Table 4.** EO performances of selected $LiNbO_3$ metasurfaces.

| Reference | Material cut | Q-factor | Dimension | $V_{pp}$ (V) | Modulation rate (MHz) | Wavelength (nm) |
|---|---|---|---|---|---|---|
| Barton *et al.*[71] | X cut | $2.8 \times 10^4$ | 4 μm, not specified in the other dimension | 30 | - | 1,397 |
| Gao *et al.*[70] | X cut | $< 10^3$ | 10 × 10 | 300 | 1 | 633 |
| Xu *et al.*[123] (only numerical) | X cut | $2.05 \times 10^4$ | unit-cell parameters: P = 0.92, H = 0.46, W = 0.30, T = 0.10 | 14 | - | 1,550.7 |
| Klopfer *et al.*[124] (only numerical) | X cut | $> 3.0 \times 10^4$ | unit cell: period = 1.0, nanobar width = 0.5, Si thickness = 0.22, LN thickness = 0.10; two nanofins, each 0.10 wide | ±25 | - | 1,564 |
| Kanyang *et al.*[125] (only numerical) | Z cut | high-Q (quasi-BICs) | unit cell: px = 0.65, py = 1.022; h = 0.80, a = 0.35, b = 0.16 | -50-150 | - | 1,463 |
| Leng *et al.*[126] (only numerical) | Z cut | 1,320 (transmission), 3,640 (reflection) | unit cell: P = 0.80, l = 0.40, hLN = 0.30, hg = 0.20, hITO = 0.05/0.20 | 40 (amplitude), 80 (phase) | - | 1,600 |
| Weigand *et al.*[72] | X cut | 129 (Exp.)272 (Sim.) | 20 × 20 | 10 | 2.5 | 774.2 |
| Jiang *et al.*[127] (only numerical) | X cut | $10^7$-$10^9$ | 1,000 × 1,000 | 1-6 | - | Telecom band |
| He *et al.*[128] | X cut | - | 10 × 10 | ±50 | 0.05 | 902 (FF), 451 (SHG) |
| Li & Ao[129] (only numerical) | Z cut | 97 | 100 × 100 | ±20 | - | 1,550 |
| Qiu *et al.*[130] (only numerical) | X cut | $> 10^4$ | Electrode gap: 10 | 15 | - | Telecom (FF) Visible (SHG) |
| Di Francescantonio *et al.*[131] | - | > 7,500 (Exp.) 11,000 (Theory) | 10 × 1,500 | 20 (Linear AC) 18 (±9 DC for SHG) | 800 (-3 dB) 1,400 (-6 dB) | ~1,553 (FF) ~776 (SHG) |

EO: electro-optic; Si: silicon; LN: lithium niobate; FF: fundamental frequency; SHG: second harmonic generation; AC: alternating current.

More recently, to mitigate the strong amplitude-phase coupling inherent in conventional resonant modulation and realize efficient pure-phase manipulation, a tunable $LiNbO_3$ metasurface based on Huygens' quasi-BICs modes was proposed[125]. In this numerical study, Kanyang *et al.* employed meticulous structural asymmetry engineering to excite spectrally overlapping electric and magnetic quasi-BICs modes. This mechanism allows minute refractive index variations to induce a full 2π phase shift near resonance while maintaining near-unity transmittance (> 96%) by suppressing back-scattering, representing an ideal unit for efficient optical phased arrays. Furthermore, to achieve synergistic control over both the amplitude and phase of the optical field, a high-Q unetched metasurface integrated with transparent indium tin oxide electrodes was proposed, as shown in Figure 7B[126]. Benefiting from the field-enhancement effects of high-Q GMRs, the device demonstrated efficient dynamic modulation in two distinct configurations: achieving a transmission amplitude modulation depth of over 60 dB at 20 V and, with the addition of a gold back-reflector, realizing a

reflection phase shift of ~1.75π (at 80 V).

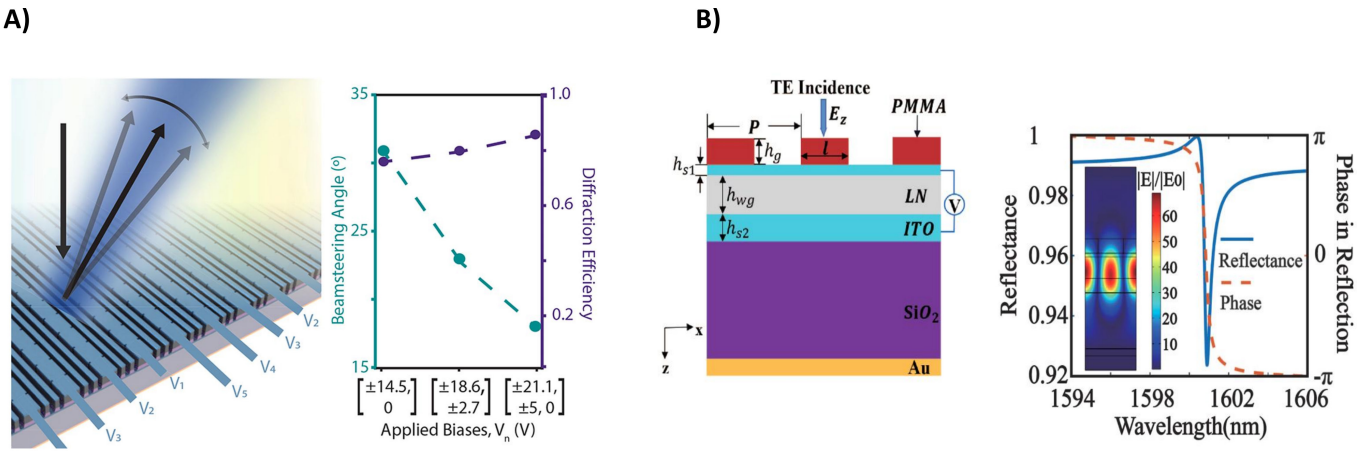


**Figure 7.** $LiNbO_3$ metasurfaces for EO phase modulation. (A) High-Q silicon-on-$LiNbO_3$ metasurface employing Fano resonances for electrically reconfigurable wavefront shaping. Reproduced with permission from reference[124]. Copyright © 2022 American Chemical Society; (B) High-Q unetched $LiNbO_3$ metasurface integrated with transparent electrodes. Adapted with permission from reference[126]. Copyright © 2024 Optica Publishing Group. EO: electro-optic; TE: transverse electric; PMMA: poly(methyl methacrylate); LN: lithium niobate; ITO: indium tin oxide.

Complementing the phase modulation schemes discussed above, resonant metasurfaces have also been exploited to achieve efficient amplitude (intensity) modulation. To overcome weak EO interactions at subwavelength scales, a Mie resonance-enhanced x-cut $LiNbO_3$ metasurface was developed, as shown in Figure 8A[72]. The design maximizes the spatial overlap integral between the RF electric field and the localized optical field within the nanopillars by optimizing electrode geometry. Physically, this approach exploits the spectral shift of Mie resonance peaks driven by refractive index changes induced by the Pockels effect, thereby converting minute refractive index perturbations into detectable optical intensity fluctuations with an 80-fold enhancement over unpatterned films. To further sharpen the resonance and improve modulation depth, mechanisms based on bound states were introduced. Jiang *et al.* utilized a corrugated $LiNbO_3$ grating to support quasi-guided modes[127]. By applying a voltage to induce a period-doubling perturbation, dispersion curves are folded, transforming guided modes into high-Q leaky resonances. Benefiting from the ultra-narrow linewidth, this scheme enables high-extinction-ratio free-space optical switching with minimal insertion loss.

Extending beyond linear intensity control, this resonant tuning concept has been powerfully applied to modulate nonlinear processes. By electro-optically shifting the fundamental resonance, the efficiency of SHG can be dynamically controlled. Work in 2024 demonstrated this concept utilizing GMRs. As shown in Figure 8B, an x-cut nanohole array was employed to enhance SHG, where an external electric field shifted the resonance condition of the pump light[128]. Since SHG intensity is highly sensitive to pump resonance, a modulation depth of 11.3% was achieved under ± 50 V, opening a new chapter in active nonlinear metadevices. Additionally, a hybrid EO metasurface integrating a doped silicon nanograting into TFLN was developed[129]. By embedding the silicon grating within the z-cut $LiNbO_3$ layer atop an aluminum reflector, Surface Plasmon Polariton modes were excited to generate a strong out-of-plane electric field. Crucially, this field orientation maximizes the overlap with the dominant $r_{33}$ coefficient, yielding a high spectral sensitivity (~0.25 nm/V) and nearly 100% modulation depth under ± 20 V.

Finally, to push the performance limits in terms of Q-factor and operation speed, nonlocal metasurfaces have emerged as a premier platform. As presented in Figure 8C[130], utilizing Brillouin Zone Folding-induced BICs, researchers achieved ultra-high-Q resonances (Q > 104) that enabled dramatic SHG modulation (> 99%) with reduced driving voltages (15 V). Culminating in a breakthrough study, efficient GHz modulation covering both linear and nonlinear regimes was demonstrated. As presented in Figure 8D[131], a nonlocal metasurface leveraging high-Q resonances (Q ≈ 8,000) not only achieved high-speed reflectance modulation in the linear region but also innovatively demonstrated the mechanism's continued effectiveness in the nonlinear regime under continuous-wave pumping. Experiments realized a SHG intensity modulation exceeding 100%, effectively addressing the trade-off where traditional metasurfaces struggle to simultaneously achieve high modulation depth, high Q-factor, and high operation speed. This represents one of the highest levels of current research in $LiNbO_3$ active metasurfaces.

## 7. Discussion and Outlook

### 7.1 Thermal stability and long-term reliability

At the same time, several practical challenges must be addressed for the translation of $LiNbO_3$ metasurfaces from proof-of-concept demonstrations to real-world applications. Although $LiNbO_3$ is chemically robust, the performance of $LiNbO_3$ metasurfaces remains susceptible to temperature fluctuations. This sensitivity primarily arises from the thermo-optic effect ($d_n/d_T$) and thermal expansion

coefficient (α), which can induce refractive-index variations, structural deformation, resonance shifts, and changes in modal overlap[132,121].

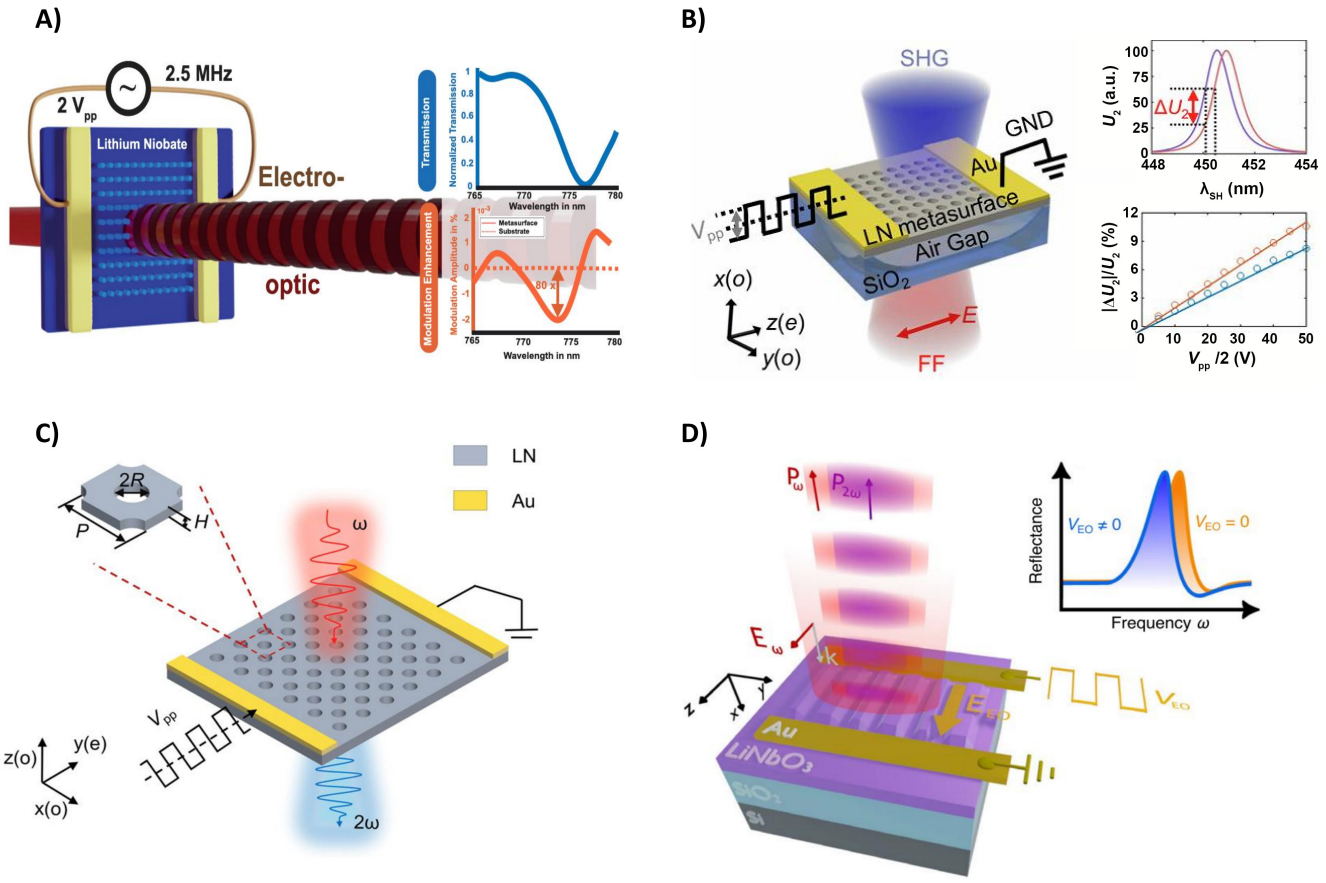


**Figure 8.** EO modulation of linear and nonlinear optical responses in $LiNbO_3$ metasurfaces. (A) Resonant EO phase-gradient metasurface based on silicon nanobars integrated on a $LiNbO_3$ substrate. Reproduced with permission from reference[72]. Copyright © 2021 American Chemical Society; (B) Low-voltage EO phase modulation scheme based on engineered quasi-BICs resonances in $LiNbO_3$ metasurfaces. Reproduced with permission from reference[128]. Copyright © 2024 American Chemical Society; (C) Electro-optically tunable nonlinear metasurface based on BZF-BICs. Reproduced with permission from reference[130]. ©2025 American Physical Society; (D) Non-local $LiNbO_3$ metasurface exhibiting GHz-rate EO modulation in both the linear and nonlinear regimes. Reproduced from reference[131]. CC BY 4.0. EO: electro-optic; BICs: bound states in the continuum; BZF-BICs: Brillouin-zone-folding-induced BICs; GHz: gigahertz; SHG: second harmonic generation; LN: lithium niobate; GND: ground.

For EO metasurfaces, which often exploit high-Q resonances such as BICs or Fano resonances, even minor temperature variations can induce a significant shift in the resonance wavelength ($\lambda_{res}$). Given that $LiNbO_3$ exhibits a thermo-optic coefficient on the order of $10^{-5}$ $K^{-1}$ near the telecom band, a temperature change of a few degrees can shift the resonance peak by tens of picometers, potentially leading to a misalignment of the operating bias point and a subsequent degradation in modulation depth[132-134]. Furthermore, long-term reliability in EO devices is challenged by "DC drift", a phenomenon where the accumulation of intrinsic or surface ions under a biased electric field creates a screening potential, thereby causing temporal fluctuations in the half-wave voltage and extinction ratio[135,75].

In the context of NLO metasurfaces, thermal stability is equally critical. Processes such as SHG or SPDC are highly dependent on maintaining precise phase-matching or resonance-matching conditions. Photothermal effects arising from localized field enhancement under high-power pump lasers can lead to self-heating, resulting in thermal detuning of the resonance and a drop in conversion efficiency[121,136]. Additionally, for TFLN integrated on silicon or silica substrates, the coefficient of thermal expansion mismatch between $LiNbO_3$ and the substrate can induce mechanical stress during extreme temperature cycling, posing a risk of film delamination or structural fatigue[137,138].

Beyond thermal and electrical factors, environmental sensitivity poses another critical challenge. The high-Q resonances of $LiNbO_3$ metasurfaces are highly susceptible to surface adsorbates, such as moisture in varying humidity environments, necessitating robust surface passivation (e.g., $Al_2O_3$ deposited by atomic layer deposition). To mitigate these stability challenges, future developments must focus on a synergy of active thermal management, passive athermal designs using compensatory cladding, and advanced surface passivation[135,75,139].

### 7.2 Fabrication yield and photonic integration

Another major engineering hurdle lies in the scalable manufacturing and system-level integration of $LiNbO_3$ metasurfaces. Unlike silicon, $LiNbO_3$ is notoriously recalcitrant to dry etching due to its chemical inertness. Standard argon-ion milling often suffers from non-volatile by-products, resulting in slanted sidewalls and increased surface roughness. These fabrication imperfections severely compromise the uniformity and fabrication yield of large-area arrays. Developing advanced etching recipes and hard-mask optimizations remains a critical ongoing research area to achieve wafer-scale, high-yield production.

Furthermore, to realize fully functional on-chip systems, the photonic integration of $LiNbO_3$ metasurfaces with other platforms is indispensable. Because $LiNbO_3$ is not an efficient light emitter, the heterogeneous integration of $LiNbO_3$ metasurfaces with on-chip light sources (e.g., III-V diode lasers) and low-loss routing waveguides (e.g., silicon nitride or silicon-on-insulator) is a prerequisite for comprehensive optical circuits. Overcoming these integration and packaging challenges, alongside employing high-thermal-conductivity substrates to enhance power handling, will ultimately bridge the gap between proof-of-concept $LiNbO_3$ metasurfaces and commercial optical systems.

### 7.3 Conclusion and perspective

In summary, this review has delineated the rapid evolution of $LiNbO_3$ metasurfaces, from fundamental fabrication breakthroughs to sophisticated applications in nonlinear frequency conversion and high-speed EO modulation. While these subwavelength architectures offer unprecedented control over light-matter interactions, transitioning from laboratory prototypes to commercial-grade photonic integrated circuits necessitates overcoming the intrinsic hurdles of thermal sensitivity, DC drift, and scalable manufacturing. Future research trajectories should prioritize the development of athermal device geometries and heterogeneous integration strategies to harness the full potential of $LiNbO_3$ in the next generation of quantum and classical optical communications.

## Declarations

### Authors contribution

Liu H, Chen X: Conceptualization, writing-original draft, writing-review & editing.
Sun H: Writing-original draft, writing-review & editing.

### Conflicts of interest

Xianfeng Chen is an Editorial Board Member of *Light Manipulation and Applications*. The other authors declare no conflicts of interest.

### Ethical approval

Not applicable.

### Consent to participate

Not applicable.

### Consent for publication

Not applicable.

### Availability of data and materials

Not applicable.

### Funding

The work was supported by the National Natural Science Foundation of China (Grant Nos. 12192252, 12341403 and 12374314), and the National Key Research and Development Program of China (Grant No. 2023YFA1407200).



## References

1. Chen HT, Taylor AJ, Yu N. A review of metasurfaces: Physics and applications. Rep Prog Phys. 2016;79(7):076401. [DOI]
2. Maiuri M, Schirato A, Cerullo G, Della Valle G. Ultrafast all-optical metasurfaces: Challenges and new frontiers. ACS Photonics. 2024;11(8):2888-2905. [DOI]

3. Yu N, Capasso F. Flat optics with designer metasurfaces. Nat Mater. 2014;13(2):139-150. [DOI]
4. Kildishev AV, Boltasseva A, Shalaev VM. Planar photonics with metasurfaces. Science. 2013;339(6125):1232009. [DOI]
5. Genevet P, Capasso F, Aieta F, Khorasaninejad M, Devlin R. Recent advances in planar optics: From plasmonic to dielectric metasurfaces. Optica. 2017;4(1):139-152. [DOI]
6. Lalanne P, Chavel P. Metalenses at visible wavelengths: Past, present, perspectives. Laser Photonics Rev. 2017;11(3):1600295. [DOI]
7. Capasso F. The future and promise of flat optics: A personal perspective. Nanophotonics. 2018;7(6):953-957. [DOI]
8. Quevedo-Teruel O, Chen H, Díaz-Rubio A, Gok G, Grbic A, Minatti G, et al. Roadmap on metasurfaces. J Opt. 2019;21(7):073002. [DOI]
9. Chen WT, Zhu AY, Capasso F. Flat optics with dispersion-engineered metasurfaces. Nat Rev Mater. 2020;5(8):604-620. [DOI]
10. Scheuer J. Optical metasurfaces are coming of age: Short- and long-term opportunities for commercial applications. ACS Photonics. 2020;7(6):1323-1354. [DOI]
11. Piccardo M, Ginis V, Forbes A, Mahler S, Friesem AA, Davidson N, et al. Roadmap on multimode light shaping. J Opt. 2022;24(1):013001. [DOI]
12. Zheludev NI, Kivshar YS. From metamaterials to metadevices. Nat Mater. 2012;11(11):917-924. [DOI]
13. Ren M, Cai W, Xu J. Tailorable dynamics in nonlinear optical metasurfaces. Adv Mater. 2020;32(3):1806317. [DOI]
14. Yu N, Genevet P, Kats MA, Aieta F, Tetienne JP, Capasso F, et al. Light propagation with phase discontinuities: Generalized laws of reflection and refraction. Science. 2011;334(6054):333-337. [DOI][PubMed]
15. Ni X, Emani NK, Kildishev AV, Boltasseva A, Shalaev VM. Broadband light bending with plasmonic nanoantennas. Science. 2012;335(6067):427. [DOI][PubMed]
16. Sun S, He Q, Xiao S, Xu Q, Li X, Zhou L. Gradient-index meta-surfaces as a bridge linking propagating waves and surface waves. Nat Mater. 2012;11(5):426-431. [DOI][PubMed]
17. Pendry JB, Schurig D, Smith DR. Controlling electromagnetic fields. Science. 2006;312(5781):1780-1782. [DOI]
18. Leonhardt U. Optical conformal mapping. Science. 2006;312(5781):1777-1780. [DOI][PubMed]
19. Cai W, Shalaev V. Optical metamaterials. New York: Springer; 2010. [DOI]
20. Zou L, Withayachumnankul W, Shah CM, Mitchell A, Bhaskaran M, Sriram S, et al. Dielectric resonator nanoantennas at visible frequencies. Opt Express. 2013;21(1):1344-1352. [DOI][PubMed]
21. Holloway CL, Kuester EF, Gordon JA, O'Hara J, Booth J, Smith DR. An overview of the theory and applications of metasurfaces: The two-dimensional equivalents of metamaterials. IEEE Antennas Propag Mag. 2012;54(2):10-35. [DOI]
22. Yu N, Genevet P, Aieta F, Kats MA, Blanchard R, Aoust G, et al. Flat optics: Controlling wavefronts with optical antenna metasurfaces. IEEE J Sel Top Quantum Electron. 2013;19(3):4700423. [DOI]
23. Walia S, Shah CM, Gutruf P, Nili H, Chowdhury DR, Withayachumnankul W, et al. Flexible metasurfaces and metamaterials: A review of materials and fabrication processes at micro- and nano-scales. Appl Phys Rev. 2015;2(1):011303. [DOI]
24. Minovich AE, Miroshnichenko AE, Bykov AY, Murzina TV, Neshev DN, Kivshar YS. Functional and nonlinear optical metasurfaces. Laser Photonics Rev. 2015;9(2):195-213. [DOI]
25. Genevet P, Capasso F. Holographic optical metasurfaces: A review of current progress. Rep Prog Phys. 2015;78(2):024401. [DOI]
26. Wang C, Li Z, Kim MH, Xiong X, Ren XF, Guo GC, et al. Metasurface-assisted phase-matching-free second harmonic generation in lithium niobate waveguides. Nat Commun. 2017;8(1):2098. [DOI][PubMed][PMC]
27. Ni X, Wong ZJ, Mrejen M, Wang Y, Zhang X. An ultrathin invisibility skin cloak for visible light. Science. 2015;349(6254):1310-1314. [DOI]
28. Glybovski SB, Tretyakov SA, Belov PA, Kivshar YS, Simovski CR. Metasurfaces: From microwaves to visible. Phys Rep. 2016;634:1-72. [DOI]
29. Li G, Zhang S, Zentgraf T. Nonlinear photonic metasurfaces. Nat Rev Mater. 2017;2:17010. [DOI]
30. Ding F, Pors A, Bozhevolnyi SI. Gradient metasurfaces: A review of fundamentals and applications. Rep Prog Phys. 2018;81(2):026401. [DOI]
31. Neshev D, Aharonovich I. Optical metasurfaces: New generation building blocks for multi-functional optics. Light Sci Appl. 2018;7:58. [DOI][PubMed][PMC]
32. Krasnok A, Tymchenko M, Alù A. Nonlinear metasurfaces: A paradigm shift in nonlinear optics. Mater Today. 2018;21(1):8-21. [DOI]
33. Phan T, Sell D, Wang EW, Doshay S, Edee K, Yang J, et al. High-efficiency, large-area, topology-optimized metasurfaces. Light Sci Appl. 2019;8:48. [DOI][PubMed][PMC]
34. Wang K, Chekhova M, Kivshar Y. Metasurfaces for quantum technologies. Phys Today. 2022;75(8):38-44. [DOI]
35. Santiago-Cruz T, Gennaro SD, Mitrofanov O, Addamane S, Reno J, Brener I, et al. Resonant metasurfaces for generating complex quantum states. Science. 2022;377(6609):991-995. [DOI][PubMed]
36. Ding F, Bozhevolnyi SI. Advances in quantum meta-optics. Mater Today. 2023;71:63-72. [DOI]
37. Klein MW, Enkrich C, Wegener M, Linden S. Second-harmonic generation from magnetic metamaterials. Science. 2006;313(5786):502-504. [DOI]
38. Zhang C, Hao F, Gao G, Liu X, Ma C, Lin Y, et al. Enhanced superconductivity in TiO epitaxial thin films. npj Quantum Mater. 2017;2:2. [DOI]
39. Liu H, Guo C, Vampa G, Zhang JL, Sarmiento T, Xiao M, et al. Enhanced high-harmonic generation from an all-dielectric metasurface. Nat Phys. 2018;14(10):1006-1010. [DOI]
40. Gao B, Ren M, Wu W, Hu H, Cai W, Xu J. Lithium niobate metasurfaces. Laser Photonics Rev. 2019;13(5):1800312. [DOI]

41. Gigli C, Leo G. All-dielectric $X^{(2)}$ metasurfaces: Recent progress. Opto-Electron Adv. 2022;5(7):210093. [DOI]
42. Vabishchevich P, Kivshar Y. Nonlinear photonics with metasurfaces. Photonics Res. 2023;11(2):B50-B64. [DOI]
43. Sharapova PR, Kruk SS, Solntsev AS. Nonlinear dielectric nanoresonators and metasurfaces: Toward efficient generation of entangled photons. Laser Photonics Rev. 2023;17(4):2200408. [DOI]
44. Kolkowski R, Hakala TK, Shevchenko A, Huttunen MJ. Nonlinear nonlocal metasurfaces. Appl Phys Lett. 2023;122(16):160502. [DOI]
45. Naik GV, Boltasseva A. A comparative study of semiconductor-based plasmonic metamaterials. Metamaterials. 2011;5(1):1-7. [DOI]
46. Boltasseva A, Atwater HA. Low-loss plasmonic metamaterials. Science. 2011;331(6015):290-291. [DOI]
47. Ye W, Zeuner F, Li X, Reineke B, He S, Qiu CW, et al. Spin and wavelength multiplexed nonlinear metasurface holography. Nat Commun. 2016;7:11930. [DOI][PubMed][PMC]
48. Gomes ASL, Maldonado M, de S Menezes L, Acioli LH, de Araújo CB, Dysart J, et al. Linear and third-order nonlinear optical properties of self-assembled plasmonic gold metasurfaces. Nanophotonics. 2020;9(4):725-740. [DOI]
49. Deng J, Tang Y, Chen S, Li K, Zayats AV, Li G. Giant enhancement of second-order nonlinearity of epsilon-near- zero medium by a plasmonic metasurface. Nano Lett. 2020;20(7):5421-5427. [DOI][PubMed]
50. Wu W, Ren M, Pi B, Cai W, Xu J. Displacement sensor based on plasmonic slot metamaterials. Appl Phys Lett. 2016;108(7):073106. [DOI]
51. Li Z, Wang C, Kong W, Wang Y, Guo Y, Li X, et al. Broadband achromatic metasurface filter for apodization imaging in the visible. Opto-Electron Eng. 2021;48(5):200466. [DOI]
52. Zhang J, Wu Y, Chen S, Gu S, Sun L, Zhou M, et al. Optimized bow-tie metasurface and its application in trace detection of lead ion. Opto-Electron Eng. 2021;48(8):210123. [DOI]
53. Li L, Liu Z, Ren X, Wang S, Su VC, Chen MK, et al. Metalens-array-based high-dimensional and multiphoton quantum source. Science. 2020;368(6498):1487-1490. [DOI][PubMed]
54. Liu J, Shi M, Chen Z, Wang S, Wang Z, Zhu S. Quantum photonics based on metasurfaces. Opto-Electron Adv. 2021;4(9):200092. [DOI]
55. Jahani S, Jacob Z. All-dielectric metamaterials. Nat Nanotechnol. 2016;11(1):23-36. [DOI][PubMed]
56. Kuznetsov AI, Miroshnichenko AE, Brongersma ML, Kivshar YS, Luk'yanchuk B. Optically resonant dielectric nanostructures. Science. 2016;354(6314):aag2472. [DOI][PubMed]
57. Liu S, Vabishchevich PP, Vaskin A, Reno JL, Keeler GA, Sinclair MB, et al. An all-dielectric metasurface as a broadband optical frequency mixer. Nat Commun. 2018;9(1):2507. [DOI][PubMed][PMC]
58. Fang C, Yang Q, Yuan Q, Gan X, Zhao J, Shao Y, et al. High-$Q$ resonances governed by the quasi-bound states in the continuum in all-dielectric metasurfaces. Opto-Electron Adv. 2021;4(6):200030. [DOI]
59. Cao T, Lian M, Chen X, Mao L, Liu K, Jia J, et al. Multi-cycle reconfigurable THz extraordinary optical transmission using chalcogenide metamaterials. Opto-Electron Sci. 2022;1(1):210010. [DOI]
60. Chang W, Li J, Luo C, Guo Z, Cao S, Fu Z, et al. Toroidal dipole resonances enhanced second-harmonic generation with shallow etching of lithium niobate metasurface. Opt Lett. 2025;50(2):630-633. [DOI][PubMed]
61. Duan H, He H, Yi Y, Wang L, Zhang Y, You S, et al. Efficient second-harmonic generation in a lithium niobate metasurface governed by high-Q magnetic toroidal dipole resonances. Opt Lett. 2024;49(19):5539-5542. [DOI]
62. Kong Y, Bo F, Wang W, Zheng D, Liu H, Zhang G, et al. Recent progress in lithium niobate: Optical damage, defect simulation, and on-chip devices. Adv Mater. 2020;32(3):e1806452. [DOI][PubMed]
63. Arizmendi L. Photonic applications of lithium niobate crystals. Phys Status Solidi A. 2004;201(2):253-283. [DOI]
64. Honardoost A, Abdelsalam K, Fathpour S. Rejuvenating a versatile photonic material: Thin-film lithium niobate. Laser Photonics Rev. 2020;14(9):2000088. [DOI]
65. Carletti L, Li C, Sautter J, Staude I, De Angelis C, Li T, et al. Second harmonic generation in monolithic lithium niobate metasurfaces. Opt Express. 2019;27(23):33391-33398. [DOI][PubMed]
66. Huang Z, Wang M, Li Y, Shang J, Li K, Qiu W, et al. Highly efficient second harmonic generation of thin film lithium niobate nanograting near bound states in the continuum. Nanotechnology. 2021;32(32):325207. [DOI][PubMed]
67. Fedotova A, Younesi M, Sautter J, Vaskin A, Löchner FJF, Steinert M, et al. Second-harmonic generation in resonant nonlinear metasurfaces based on lithium niobate. Nano Lett. 2020;20(12):8608-8614. [DOI]
68. Carletti L, Zilli A, Moia F, Toma A, Finazzi M, De Angelis C, et al. Steering and encoding the polarization of the second harmonic in the visible with a monolithic $LiNbO_3$ metasurface. ACS Photonics. 2021;8(3):731-737. [DOI][PubMed][PMC]
69. Ma J, Xie F, Chen W, Chen J, Wu W, Liu W, et al. Nonlinear lithium niobate metasurfaces for second harmonic generation. Laser Photonics Rev. 2021;15(5):2000521. [DOI]
70. Gao B, Ren M, Wu W, Cai W, Xu J. Electro-optic lithium niobate metasurfaces. Sci China Phys Mech Astron. 2021;64(4):240362. [DOI]
71. Barton D, Lawrence M, Dionne J. Wavefront shaping and modulation with resonant electro-optic phase gradient metasurfaces. Appl Phys Lett. 2021;118(7):071104. [DOI]
72. Weigand H, Vogler-Neuling VV, Escalé MR, Pohl D, Richter FU, Karvounis A, et al. Enhanced electro-optic modulation in resonant metasurfaces of lithium niobate. ACS Photonics. 2021;8(10):3004-3009. [DOI]
73. Poberaj G, Hu H, Sohler W, Günter P. Lithium niobate on insulator (LNOI) for micro-photonic devices. Laser Photonics Rev. 2012;6(4):488-503. [DOI]
74. Boes A, Corcoran B, Chang L, Bowers J, Mitchell A. Status and potential of lithium niobate on insulator (LNOI) for photonic integrated circuits. Laser Photonics Rev. 2018;12(4):1700256. [DOI]

75. Zhu D, Shao L, Yu M, Cheng R, Desiatov B, Xin CJ, et al. Integrated photonics on thin-film lithium niobate. Adv Opt Photon. 2021;13(2):242-352. [DOI]
76. Jia Y, Wang L, Chen F. Ion-cut lithium niobate on insulator technology: Recent advances and perspectives. Appl Phys Rev. 2021;8(1):011307. [DOI]
77. Si G, Danner AJ, Teo SL, Teo EJ, Teng J, Bettiol AA. Photonic crystal structures with ultrahigh aspect ratio in lithium niobate fabricated by focused ion beam milling. J Vac Sci Technol B. 2011;29(2):021205. [DOI]
78. Ulliac G, Calero V, Ndao A, Baida FI, Bernal MP. Argon plasma inductively coupled plasma reactive ion etching study for smooth sidewall thin film lithium niobate waveguide application. Opt Mater. 2016;53:1-5. [DOI]
79. Timpu F, Sendra J, Renaut C, Lang L, Timofeeva M, Buscaglia MT, et al. Lithium niobate nanocubes as linear and nonlinear ultraviolet Mie resonators. ACS Photonics. 2019;6(2):545-552. [DOI]
80. Wang J, Liu Z, Xiang J, Chen B, Wei Y, Liu W, et al. Ultraviolet second harmonic generation from Mie-resonant lithium niobate nanospheres. Nanophotonics. 2021;10(17):4273-4278. [DOI]
81. Savo R, Morandi A, Müller JS, Kaufmann F, Timpu F, Reig Escalé M, et al. Broadband Mie driven random quasi-phase-matching. Nat Photonics. 2020;14(12):740-747. [DOI]
82. Ali RF, Gates BD. Lithium niobate particles with a tunable diameter and porosity for optical second harmonic generation. RSC Adv. 2021;12(2):822-833. [DOI][PubMed][PMC]
83. Kamali AR, Fray DJ. Preparation of lithium niobate particles via reactive molten salt synthesis method. Ceram Int. 2014;40(1):1835-1841. [DOI]
84. Wang Y, Zhou XY, Chen Z, Cai B, Ye ZZ, Gao CY, et al. Synthesis of cubic $LiNbO_3$ nanoparticles and their application *in vitro* bioimaging. Appl Phys A. 2014;117(4):2121-2126. [DOI]
85. Wood BD, Mocanu V, Gates BD. Solution-phase synthesis of crystalline lithium niobate nanostructures. Adv Mater. 2008;20(23):4552-4556. [DOI]
86. Mohanty D, Chaubey GS, Yourdkhani A, Adireddy S, Caruntu G, Wiley JB. Synthesis and piezoelectric response of cubic and spherical $LiNbO_3$ nanocrystals. RSC Adv. 2012;2(5):1913-1916. [DOI]
87. Ali RF, Gates BD. Synthesis of lithium niobate nanocrystals with size focusing through an Ostwald ripening process. Chem Mater. 2018;30(6):2028-2035. [DOI]
88. Kim E, Steinbrück A, Buscaglia MT, Buscaglia V, Pertsch T, Grange R. Second-harmonic generation of single $BaTiO_3$ nanoparticles down to 22 nm diameter. ACS Nano. 2013;7(6):5343-5349. [DOI][PubMed]
89. Karvounis A, Vogler-Neuling VV, Richter FU, Dénervaud E, Timofeeva M, Grange R. Electro-optic metasurfaces based on barium titanate nanoparticle films. Adv Opt Mater. 2020;8(17):2000623. [DOI]
90. Talts ÜL, Weigand H, Occhiodori I, Grange R. Scalable lithium niobate nanoimprinting for nonlinear metalenses. Adv Mater. 2025;37(27):e2418957. [DOI][PubMed][PMC]
91. Lin J, Yao N, Hao Z, Zhang J, Mao W, Wang M, et al. Broadband quasi-phase-matched harmonic generation in an on-chip monocrystalline lithium niobate microdisk resonator. Phys Rev Lett. 2019;122(17):173903. [DOI][PubMed]
92. Lehr D, Reinhold J, Thiele I, Hartung H, Dietrich K, Menzel C, et al. Enhancing second harmonic generation in gold nanoring resonators filled with lithium niobate. Nano Lett. 2015;15(2):1025-1030. [DOI][PubMed]
93. Kim KH, Rim WS. Anapole resonances facilitated by high-index contrast between substrate and dielectric nanodisk enhance vacuum ultraviolet generation. ACS Photonics. 2018;5(12):4769-4775. [DOI]
94. Liu Y, Wang B, Hu L, Li C, Ji X, Geng G, et al. Observation of anapole resonances in lithium niobate metasurfaces with significantly enhanced second harmonic generation. Adv Mater Technol. 2024;9(22):2400318. [DOI]
95. Li Z, Hu Z, Ye X, Mao Z, Feng J, Li H, et al. Enhanced second-harmonic generation in thin-film lithium niobate circular Bragg nanocavity. Nano Lett. 2024;24(37):11676-11682. [DOI][PubMed]
96. Kang L, Bao H, Werner DH. Efficient second-harmonic generation in high $Q$-factor asymmetric lithium niobate metasurfaces. Opt Lett. 2021;46(3):633-636. [DOI][PubMed]
97. Zhang X, He L, Gan X, Huang X, Du Y, Zhai Z, et al. Quasi-bound states in the continuum enhanced second-harmonic generation in thin-film lithium niobate. Laser Photonics Rev. 2022;16(9):2200031. [DOI]
98. Liu R, Zhou C. Second harmonic generation in an anisotropic lithium niobate metasurface governed by quasi-BICs. Opt Lett. 2023;48(24):6565-6568. [DOI]
99. Qu L, Bai L, Jin C, Liu Q, Wu W, Gao B, et al. Giant second harmonic generation from membrane metasurfaces. Nano Lett. 2022;22(23):9652-9657. [DOI][PubMed]
100. Yuan S, Wu Y, Dang Z, Zeng C, Qi X, Guo G, et al. Strongly enhanced second harmonic generation in a thin film lithium niobate heterostructure cavity. Phys Rev Lett. 2021;127(15):153901. [DOI][PubMed]
101. Zhao Y, Chen Z, Wang C, Yang Y, Sun HB. Efficient second- and higher-order harmonic generation from $LiNbO_3$ metasurfaces. Nanoscale. 2023;15(31):12926-12932. [DOI][PubMed]
102. Wang Z, Li B, Lu N, Han Z, Xu L, Rahmani M, et al. Highly efficient ultraviolet harmonic generation based on coupled guided mode resonances in lithium niobate metasurfaces. Laser Photonics Rev. 2025;19(22):e01010. [DOI]
103. Huang Z, Luo K, Feng Z, Zhang Z, Li Y, Qiu W, et al. Resonant enhancement of second harmonic generation in etchless thin film lithium niobate heteronanostructure. Sci China Phys Mech Astron. 2022;65(10):104211. [DOI]

104. Fang C, Kanyang R, Ji Y, Zhang Y, Yang J, Wang D, et al. Multiple high-*Q* optical modes in a polymer-lithium niobate integrated metasurface. Laser Photonics Rev. 2024;18(2):2300900. [DOI]
105. Jiang H, Sun K, Jia Y, Cai Y, Levy U, Han Z. Tunable second harmonic generation with large enhancement in a nonlocal all-dielectric metasurface over a broad spectral range. Adv Opt Mater. 2024;12(17):2303229. [DOI]
106. Valencia Molina L, Camacho Morales R, Zhang J, Schiek R, Staude I, Sukhorukov AA, et al. Enhanced infrared vision by nonlinear up-conversion in nonlocal metasurfaces. Adv Mater. 2024;36(31):2402777. [DOI]
107. Li L, Qu L, Wu W, Li C, Bai L, Wang C, et al. Optimizing second harmonic generation in metasurfaces: The mode overlap factor. Laser Photonics Rev. 2026;20(6):e01098. [DOI]
108. Hu L, Wang B, Guo Y, Du S, Chen J, Li J, et al. Quasi-BIC enhanced broadband terahertz generation in all-dielectric metasurface. Adv Opt Mater. 2022;10(12):2200193. [DOI]
109. Santiago-Cruz T, Fedotova A, Sultanov V, Weissflog MA, Arslan D, Younesi M, et al. Photon pairs from resonant metasurfaces. Nano Lett. 2021;21(10):4423-4429. [DOI]
110. Zhang J, Ma J, Parry M, Cai M, Camacho-Morales R, Xu L, et al. Spatially entangled photon pairs from lithium niobate nonlocal metasurfaces. Sci Adv. 2022;8(30):eabq4240. [DOI][PubMed][PMC]
111. Ma J, Zhang J, Jiang Y, Fan T, Parry M, Neshev DN, et al. Polarization engineering of entangled photons from a lithium niobate nonlinear metasurface. Nano Lett. 2023;23(17):8091-8098. [DOI]
112. Chen S, Li Z, Zhang Y, Cheng H, Tian J. Phase manipulation of electromagnetic waves with metasurfaces and its applications in nanophotonics. Adv Opt Mater. 2018;6(13):1800104. [DOI]
113. Chen S, Liu W, Li Z, Cheng H, Tian J. Metasurface-empowered optical multiplexing and multifunction. Adv Mater. 2020;32(3):e1805912. [DOI][PubMed]
114. Liu Y, Wang B, et al. Ultraviolet metalens based on nonlinear wavefront manipulation of lithium niobate metasurfaces. ACS Photonics. 2025;12(4):1857-1864. [DOI]
115. Mekhael M, Stolt T, Weigand H, Arola K, Grange R, Genevet P, et al. Wavelength-selective nonlinear wavefront control in resonant thin-film lithium niobate metasurfaces. arXiv:2601.21382 [Preprint]. 2026. [DOI]
116. Shaltout AM, Shalaev VM, Brongersma ML. Spatiotemporal light control with active metasurfaces. Science. 2019;364(6441):eaat3100. [DOI]
117. Abdelraouf OAM, Wang Z, Liu H, Dong Z, Wang Q, Ye M, et al. Recent advances in tunable metasurfaces: Materials, design, and applications. ACS Nano. 2022;16(9):13339-13369. [DOI][PubMed]
118. Nicholls LH, Rodríguez-Fortuño FJ, Nasir ME, Córdova-Castro RM, Olivier N, Wurtz GA, et al. Ultrafast synthesis and switching of light polarization in nonlinear anisotropic metamaterials. Nat Photonics. 2017;11(10):628-633. [DOI]
119. Yin X, Schäferling M, Michel AU, Tittl A, Wuttig M, Taubner T, et al. Active chiral plasmonics. Nano Lett. 2015;15(7):4255-4260. [DOI]
120. Duan X, Kamin S, Liu N. Dynamic plasmonic colour display. Nat Commun. 2017;8:14606. [DOI][PubMed][PMC]
121. Hu Y, Zhu D, Lu S, Zhu X, Song Y, Renaud D, et al. Integrated electro-optics on thin-film lithium niobate. Nat Rev Phys. 2025;7(5):237-254. [DOI]
122. Weiss A, Frydendahl C, Bar-David J, Zektzer R, Edrei E, Engelberg J, et al. Tunable metasurface using thin-film lithium niobate in the telecom regime. ACS Photonics. 2022;9(2):605-612. [DOI]
123. Xu Y, Zhang L, Du B, Chen H, Hou Y, Li T, et al. Quasi-BIC based low-voltage phase modulation on lithium niobite metasurface. IEEE Photonics Technol Lett. 2022;34(20):1077-1080. [DOI]
124. Klopfer E, Dagli S, Barton D 3rd, Lawrence M, Dionne JA. High-quality-factor silicon-on-lithium niobate metasurfaces for electro-optically reconfigurable wavefront shaping. Nano Lett. 2022;22(4):1703-1709. [DOI][PubMed]
125. Kanyang R, Fang C, Wang Y, Li X, Zeng X, Liu Y, et al. Tunable lithium niobate metasurfaces for phase-only modulation based on quasi-bound states in the continuum. Sci China Inf Sci. 2024;67(11):219401. [DOI]
126. Leng R, Chen X, Liu P, Zhu Z, Zhang J. High *Q* lithium niobate metasurfaces with transparent electrodes for efficient amplitude and phase modulation. Appl Opt. 2024;63(12):3156-3161. [DOI][PubMed]
127. Jiang H, Maqbool E, Han Z. Efficient free-space optical switching harnessing quasi-guided modes in a corrugated lithium niobate grating. Results Phys. 2024;59:107555. [DOI]
128. He Z, Qu L, Wu W, Liu J, Jin C, Wang C, et al. Electro-optically modulated nonlinear metasurfaces. Nano Lett. 2024;24(45):14215-14221. [DOI][PubMed]
129. Li H, Ao X. Electro-optic metasurfaces with silicon grating in thin-film lithium niobate. Opt Commun. 2025;592:132220. [DOI]
130. Qiu H, Tu X, Qin M, Wu F, Liu T, Xiao S. Electro-optically tunable second-harmonic generation in lithium niobate metasurfaces boosted by Brillouin zone folding induced bound states in the continuum. Phys Rev B. 2025;112(8):085418. [DOI]
131. Di Francescantonio A, Sabatti A, Weigand H, Bailly-Rioufreyt E, Vincenti MA, Carletti L, et al. Efficient GHz electro-optical modulation with a nonlocal lithium niobate metasurface in the linear and nonlinear regime. Nat Commun. 2025;16(1):7000. [DOI][PubMed][PMC]
132. Jundt DH. Temperature-dependent Sellmeier equation for the index of refraction, n(e), in congruent lithium niobate. Opt Lett. 1997;22(20):1553-1555. [DOI][PubMed]
133. Li M, Ling J, He Y, Javid UA, Xue S, Lin Q. Lithium niobate photonic-crystal electro-optic modulator. Nat Commun. 2020;11:4123. [DOI]
134. Wang C, Zhang M, Chen X, Bertrand M, Shams-Ansari A, Chandrasekhar S, et al. Integrated lithium niobate electro-optic modulators operating at CMOS-compatible voltages. Nature. 2018;562(7725):101-104. [DOI]

135. Shi J, Ye Z, Liu Z, Yan Z, Jia K, Zhang L, et al. Alleviation of DC drift in a thin-film lithium niobate modulator utilizing $Ar^+$ ion milling. Opt Lett. 2025;50(5):1703-1706. [DOI]
136. Briggs I, Chen P, Fan L. Precise wavelength alignment of second-harmonic generation in thin-film lithium niobate resonators. Opt Lett. 2024;49(23):6637-6640. [DOI][PubMed]
137. Takigawa R, Higurashi E, Suga T, Kawanishi T. Room-temperature transfer bonding of lithium niobate thin film on micromachined silicon substrate with Au microbumps. Sens Actuators A Phys. 2017;264:274-281. [DOI]
138. Xu X, Chong TC, Solanki S, Liang X, Yuan S. Anisotropic thermal expansion of stoichiometric lithium niobate crystals grown along the normal direction of facets. Opt Mater. 2004;26(4):489-494. [DOI]
139. Han P, Yang L, Xu L, Zhou X, Cai L, Agarwal AM, et al. Broadband athermal lithium niobate microresonators across C and L bands. J Lightwave Technol. 2024;42(9):3246-3250. [DOI]

## Publisher's Note